

Impulsively Started Flow in a Submarine Canyon: Comparison of Results from Laboratory and Numerical Models*

NICOLAS PÉRENNE

Environmental Fluid Dynamics Program, Department of Mechanical and Aerospace Engineering, Arizona State University, Tempe, Arizona

J. WILLIAM LAVELLE

NOAA/Pacific Marine Environmental Laboratory, Seattle, Washington

DAVID C. SMITH IV AND DON L. BOYER

Environmental Fluid Dynamics Program, Department of Mechanical and Aerospace Engineering, Arizona State University, Tempe, Arizona

(Manuscript received 13 July 2000, in final form 2 March 2001)

ABSTRACT

Intercomparisons have been made of results from laboratory experiments and a numerical model for the flow in the vicinity of an idealized submarine canyon located along an otherwise continuous shelf. Motion in the rotating and continuously stratified fluid was impulsively generated by suddenly changing the period of rotation, so that the resulting flow occurred with the coastline either on the left (upwelling favorable) or right (downwelling favorable) when facing downstream. A principal purpose of the study was to further develop the notion that laboratory experiments can be effectively utilized to provide datasets to benchmark the development of numerical models. Laboratory data are of two types: velocity fields on three horizontal planes at numerous times, and time series of isopycnal movement in the canyon area. Comparison of numerical and laboratory results shows that values for bottom friction and interior mixing in the numerical model are crucial. Once those friction/mixing parameters are set, "skill" statistics using observed and predicted horizontal velocity components indicate that the high quality of the numerical model description is maintained over the full measurement period. Two principal features of the circulation are early (<one rotation period) along-canyon flow followed by generation of a canyon vortex. In up- (down-) welling cases, the cyclone (anticyclone) develops along the upstream edge of the canyon and then advects into the canyon interior without significant local vortex stretching within the canyon itself. Numerical results for the case of an extra slow rotation rate change show that vortex creation is not an artifact of the fast rate of rotation change. The canyon vortices extend from just slightly above shelf depth to the deepest part of the canyon; the intensities of the up- and downwelling vortices are asymmetric with respect to the direction of forcing at shelf level, but basically symmetric deeper in the canyon. Upper column vorticity generation by stretching over the canyon rim and flow separation around the canyon headlands could explain this upper water column asymmetric response. The symmetric response in the lower water column is shown to be related to the flow separation only.

Overall, the results demonstrate that laboratory and numerical experiments work hand in hand to decipher the complexities of circulation and hydrography undergoing rapid change in a model coastal canyon.

1. Introduction

One of the motivations of the present study was the article by Haidvogel and Beckman (1998) on the com-

parison of numerical model results for mean flow generated by oscillatory wind stress in the vicinity of a submarine canyon incised in an otherwise continuous shelf. That study demonstrated, for seemingly identical initial and boundary conditions, that a range of coastal models gave significantly different and, in some regards, diverging results for both homogeneous and continuously stratified fluids. The disparity of those results raises the question as to how to obtain datasets that can be used as benchmarks for development and testing of numerical models.

Because data with sufficient spatial and temporal res-

* NOAA/Pacific Marine Environmental Laboratory Contribution Number 2170.

Corresponding author address: Dr. Don L. Boyer, Department of Mechanical and Aerospace Engineering, College of Engineering and Applied Sciences, Box 876106, Arizona State University, Tempe, AZ 85287-6106.

E-mail: don.boyer@asu.edu

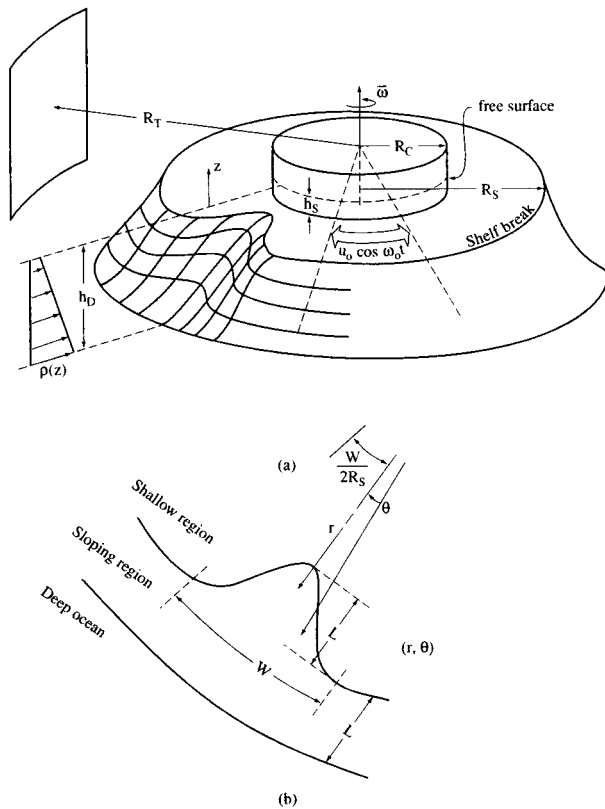


FIG. 1. Physical configuration of the experiments: (a) schematic diagram and (b) top view.

olution are difficult to obtain from oceanic field experiments and because actual ocean currents are simultaneously forced by a number of processes, providing a well-defined quantitative test for numerical models using real ocean data is nearly impossible. The need for real data to test models is even more critical when one realizes that numerical models are the only realistic approach for developing prognostic models for the ocean environment generally and the coastal region, in particular. The thesis developed here is that carefully designed and executed laboratory experiments could be useful in providing detailed data in space and time to guide the development and improvement of numerical coastal circulation models. Our view is not that a numerical model that tests well against laboratory data is thereby certified for use without caution on ocean problems. We do believe, however, that a numerical model that cannot favorably address data from controlled laboratory experiments has little chance of success when applied at full scale, especially if these experiments are conducted in the laboratory with as good an oceanic similitude as is possible. Indeed one of the basic tenants of this approach is that laboratory models can capture many of the physical conditions associated with the real oceanic flow to be simulated, for example, background rotation and stratification, complex bathymetry, and unsteady forcing as associated with tides, storm systems, etc. Other pa-

pers comparing laboratory and numerical model results for regional- to large-scale ocean problems involving effects of topography and/or stratification have appeared only recently. These include works of Pedlosky et al. (1997), Kliem and Pietrzak (1999), McClimans et al. (2000), Sanson and van Heijst (2000), and Pérenne et al. (2001, hereafter PHB).

In the present experiments we consider the case of laboratory fluid on a rotating table forced by an impulsive increase (decrease) of the table's rotation rate, leading to a downwelling (upwelling) favorable flow across a coastal canyon incised into continental slope isobaths. In a separate study (PHB), two of us also considered the case of stratified, rotating flow over the same canyon topography but with fluid forced by periodic changes of the table's rotation rate. In that study the focus was on residual flows generated by nonlinearities of the system. In the laboratory experiments reported here, we obtained detailed measurements of velocity fields during flow development and subsequent spinup (-down) of the fluid to solid-body rotation at the new rotation rate. A finite-difference numerical model was configured and forced in an analogous way. The two types of results are then compared, employing various measures whereby objective comparisons can be made between laboratory and numerical model results.

Apart from the issue of using laboratory data as a benchmark for numerical modeling, the motivation for attempting to obtain a better understanding of the motion fields in the vicinity of submarine canyons is that these are important and ubiquitous features of the coastlines of the world's oceans. Canyons play a large role in cross-shelf transport of passive material such as aquatic biota and pollutants. Furthermore, they are important locations for human activities such as fisheries, a potential source of coastal-trapped waves and internal tides, and a source of strong oceanic turbulence, which can play a role in the momentum balance of the oceans and generate intrusions of mixed fluid.

The literature on submarine canyons is growing but was still considered remarkably sparse a few years ago (Hickey 1997). Comparisons of numerical model results (Allen 1996; Klinck 1996) with in situ measurements (Hickey 1997) have focused on upwelling favorable systems and exhibited some areas of convergence but also some noticeable discrepancies, for example, evidence for closed streamlines in in situ measurements but not in numerical results (Hickey 1997). However, a recent numerical study (She and Klinck 2000) showed that a cyclonic eddy was indeed spun up inside the canyon under upwelling favorable forcing. The transition from a uniform upwelling flow inside the canyon (i.e., Freeland and Denman 1982) to a detached flow situation (where a countercurrent develops along the upstream wall of the canyon) is precisely one of the issues addressed here. The influence of flow direction (upwelling or downwelling favorable forcing) will be also shown and interpreted.

The plan for this paper is to follow these introductory remarks with a brief discussion of the laboratory facility and experimental techniques employed as well as to provide a general description of the finite-difference numerical model. Oceanic similitude will also be noted at various points because ultimately the need for accurate real ocean models motivates this work. We then compare the laboratory and numerical model results. We show the importance of bottom friction and interior mixing coefficients in controlling flow; we highlight the two major circulation features, that is, initial along-axis surges and subsequent canyon eddy development; and we quantify the likeness of laboratory and numerical results using skill measures. The time evolution of vorticity in the numerical model is shown to illustrate the mechanisms responsible for canyon eddy formation and these are contrasted with those seen in previous studies. Conclusions drawn from the comparisons and analyses are presented in the final section.

2. Experimental design and execution

The laboratory and numerical experiments consider the flow of a rotating, linearly stratified fluid past a submarine canyon incised into shelf geometry. The geometry investigated is depicted schematically in Fig. 1a, where (r, θ, z) is a cylindrical coordinate system with $r = 0$, the system center; $z = 0$, the free surface; and h , the depth of the topography from $z = 0$. The bathymetry away from the canyon is given by

$$\begin{aligned} h &= 0, & r &\leq R_C, \\ h &= h_S, & R_C &\leq r \leq R_S, \\ h &= h_D - (h_D - h_S) \cos^2 \left[\frac{\pi(r - R_S)}{2(R_D - R_S)} \right], & R_S &\leq r \leq R_D, \\ h &= h_D, & R_D &\leq r \leq R_T, \end{aligned} \quad (1)$$

where R_C , R_S , R_D , and R_T equal 0.35, 0.55, 0.70, and 0.90 m; and h_S and h_D equal 0.025 and 0.125 m, respectively. The canyon is superimposed on this topography of revolution as in Boyer et al. (2000), where the depth function in the canyon region is given by

$$\begin{aligned} h &= h_D - (h_D - h_S) \cos^2 \left[\frac{\pi(r - R_S)}{2r_Q} \right], \\ r_S &\leq r \leq R_D, & -\frac{W}{2R_S} &\leq \theta \leq \frac{W}{2R_S}, \\ r_S &= R_S - L \cos^2 \left(\frac{\pi\theta R_S}{W} \right), \\ r_Q &= (R_D - R_S) + L \cos^2 \left(\frac{\pi\theta R_S}{W} \right), \end{aligned} \quad (2)$$

where W (0.2 m) and L (0.15 m) are the nominal width and length of the canyon; see Fig. 1b.

In preparation for later comments on ocean similitude, the experimental setup is now characterized in nondimensional form. Geometry introduces several dimensionless parameters, including W/h_D and W/L , the vertical and horizontal aspect ratios, and h_S/h_D , the fractional depth of the shelf. The physical system is further characterized by the following dynamical parameters (Rossby, Burger, and Ekman numbers):

$$\text{Ro} = \frac{U}{fW} \quad \text{Bu} = \frac{N^2 h_D^2}{f^2 W^2} \quad \text{Ek} = \frac{\nu}{f h_S^2}, \quad (3)$$

where U is the characteristic velocity at the shelf break [i.e., $U = (\Delta\Omega)R_S$; see below], $f = 2\Omega_1$ is the Coriolis parameter, $N^2 = -(g/\rho_0 d\bar{\rho}/dz)$ is the square of the Brunt-Väisälä frequency, g is the acceleration due to gravity, ρ_0 is a reference density, and $\bar{\rho}(z)$ is the background density profile. The upwelling and downwelling favorable experiments considered here were performed at the following parameter values: $\text{Ro} = 0.1$, $\text{Bu} = 10$, and $\text{Ek} = 3 \times 10^{-3}$.

The oceanic relevance of experiments such as these, conducted at small Rossby number and large Burger number, is discussed in detail in PHB. Model scales were chosen specifically so that laboratory flow in and around the canyon would have similitude to typical coastal ocean canyon flows. Exact similitude is not possible, but many of the laboratory parameters are reasonably close to prototypical ocean values; for example, the fractional depth $h_S/h_D = 0.20$. The model horizontal aspect ratio W/L is higher than for a typical submarine canyon, for which $W \sim 7$ km and $L \sim 15$ km. Apart from that, the vertical scale of the topography is clearly exaggerated relative to any oceanic counterpart. This, however, is allowed by the similarity analysis if the flow is hydrostatic: in that case, the parameter h_D/W does not appear in the nondimensional equations and thus is not a similarity requirement. If the flow is able to react at the smallest timescale present in the forcing (i.e., 1 s; see below) then some nonhydrostatic transients are likely to be generated. The good match of these data with the (hydrostatic) numerical results, as documented below, shows that such transients, if generated, do not significantly modify the flow. Furthermore, two indices of nonhydrostaticity, which were derived in Boyer et al. (2000) for the case of a periodic forcing, are both much smaller than one. The first $(h_D/W)^2 \text{Ro}^2/\text{Bu} = 4 \times 10^{-4}$ does not depend on the timescale of the flow and is very small in experiments reported here. The second, $(h_D/W)^2 \text{RoRo}_T/\text{Bu} = 5 \times 10^{-2}$, where $\text{Ro}_T = (2\pi/T)/f$ and where T , a characteristic timescale of the flow, equals 1 s (the worst-case situation).

The principal aspect of the present configuration that does not match oceanic conditions is the impulsive start of the flow. Nevertheless, this set of experiments does give detailed results that can be used to calibrate nu-

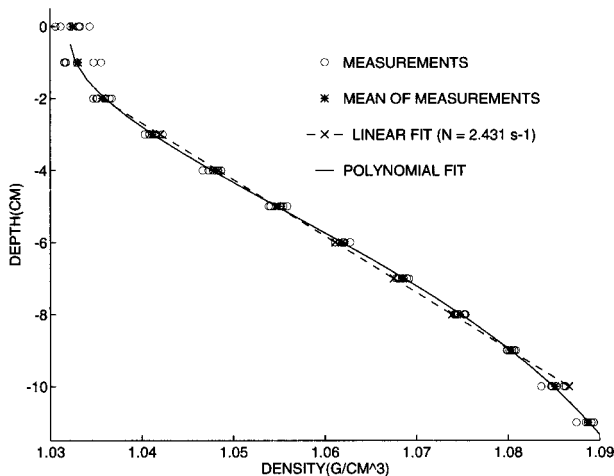


FIG. 2. Vertical density profiles measured prior to experiments. A linear interpolation of the average background profile (*'s) in the range $-10 < z < -2$ cm, gives a typical Brunt–Väisälä frequency, which is close to 2.5 s^{-1} (×'s); the analytical profile fitting the average background profile, which was used to initialize the numerical model, is also shown (solid curve).

merical experiments. Furthermore, the flow behavior of this laboratory/numerical model well after the impulsive start may also provide some insight into characteristic flow features one might expect to observe in the vicinity of isolated oceanic canyons. This last possibility may require that the quasi-steady flow field that develops inside the canyon long after offshore velocities have reached their nominal value has little memory of initial conditions or of the way the flow was established. Some results relevant to this issue will be given in section 3b(1).

a. Laboratory experiments

To prepare for an experiment, the tank was first filled with an approximately linearly stratified fluid using the, now-standard, “two bucket” method. The fluid was then set in solid-body rotation at the (anticlockwise) turntable rotation rate Ω_0 . This was attained by slowly increasing the rotation rate to ensure that mixing of the test fluid stratification was minimized during the process. The background stratification was then measured using conductivity probes: see Fig. 2, which depicts density profiles obtained for all of the experiments reported here. As one can note, density profiles are quite linear except near the surface and the bottom, where vertical mixing occurs owing to, for example, evaporation of water along the free surface and velocity shear along the bottom. The density profile used for the numerics was determined by taking the mean of all of the density profiles for the present experimental set and then fitting a polynomial to the mean values; see Fig. 2.

With the stratified fluid now in solid-body rotation, motion relative to the canyon was then established by

impulsively changing the rotation rate of the turntable. To investigate upwelling and downwelling favorable flows (i.e., with the coast on the left or right, facing downstream), the turntable rotation rate was either decreased or increased. The magnitude of the change in rotation rate (7.2%) was chosen so that the amplitude of the azimuthal velocity forced at the radius of the shelf break was equal to $U = 1 \text{ cm s}^{-1}$ for both cases. Furthermore, in order to have identical final rotation rates (so that the Rossby numbers would be the same), initial rates Ω_0 were set at 0.269 and 0.232 s^{-1} for upwelling and downwelling experiments, respectively. Rotation rates were changed linearly from Ω_0 to Ω_1 over a 1-s period.

Preliminary checks on the quality of the solid-body rotation indicated that an imperfect alignment of the axis of rotation and the vertical caused oscillations in the tank. Modifications to the apparatus were consequently made to ensure alignment within 10^{-4} rad, but some weak periodic motions were nonetheless encountered. Since those motions had a period of T_R , the period of the turntable, they were easily detected. With the improved alignment of the table, the maximum excursion distance of isopycnals in the tank owing to the residual misalignment was estimated to be $\sim 0.1\text{--}0.3$ mm; this excursion level was considered tolerable. In further pursuit of error reduction, a lid was affixed to the tank a few centimeters above the fluid surface to prevent the immobile air of the laboratory from exerting a surface “wind stress” on the working fluid. Velocities measured for constant Ω showed residual currents with amplitudes of $\sim 0.2\text{--}0.3 \text{ mm s}^{-1}$, a level also considered acceptable.

Data taken in the laboratory were of two types: (i) times series of conductivity in the canyon at fixed points and (ii) (Eulerian) velocity fields in horizontal planes at selected elevations.

Conductivity fluctuations, sampled with a frequency of 10 Hz and low-pass filtered at 1 Hz, were recorded by four rack-mounted probes immersed to various depths in the fluid at horizontal locations 1, 2, 3, and 4 shown in Fig. 3a. Vertical exploration of the density field was accomplished by repositioning the rack with depth and sampling several identically configured experiments. Data were taken at standard depths $z_1 = -1.25$ cm, $z_2 = -2.5$ cm, and $z_3 = -5$ cm (see Fig. 3b). The probe measurements were calibrated directly against density using hydrometers. The vertical displacement η of isopycnals at any probe site was inferred from the density time series using the relationship

$$\Delta\eta(t) = \frac{[\rho(t) - \bar{\rho}]}{-\frac{d\rho}{dz}}, \quad (4)$$

where $\bar{\rho}(z)$ is the background density gradient measured prior to the experiment. The equation of state used is $\rho = 0.998 + 7.98 \times 10^{-4} \text{ S g cm}^{-3}$. Probe data were

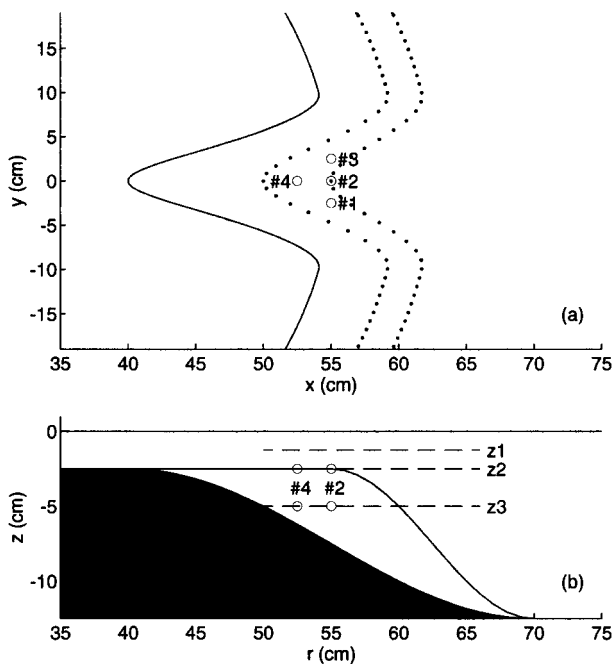


FIG. 3. Schematic diagram of locations of conductivity probes and horizontal velocity measurements: (a) plan view, where the shelf-break (solid line) and the $z = -5$ cm and $z = -7.5$ cm isobaths (dotted lines) are shown; (b) vertical cross section—the topographic profile of the canyon is shown by the black-shaded region, while the continental slope is shown by the curved solid boundary.

synchronously recorded with the timing signal from the computer controlling the rotation rate of the turntable. Consequently, the phase of density fluctuations relative to changes in Ω is accurately known. The time at which the rotation rate begins to change in each experiment is hereafter designated as $t = 0$.

The velocity field along horizontal planes was inferred from the analysis of sequential digital images of particles suspended in the fluid. A horizontal light sheet was projected through the fluid at the various levels defined above; these levels were explored in separate experiments, using a standard light source. The light sheet was a few millimeters thick and the field of view extended typically over 30×25 cm². The fluid was seeded with neutrally buoyant particles and their motion was filmed from above and recorded on an S-VHS videotape recorder. The tracking was performed with polystyrene particles of density 1.04 ± 0.005 g cm⁻³. This rather broad range of densities allowed particles to float at various levels in the continuously stratified fluid; thus, some particles were always present in the light sheet despite the fact that particles can move vertically as well as horizontally.

Videotapes were processed using the Digimage software (Dalziel 1992). Digimage allows for (i) the identification of particles present in the field of view; (ii) the tracking of these particles using a sophisticated, cost-minimizing algorithm; and (iii) the interpolation/

averaging of the resulting randomly spaced Lagrangian velocity measurements onto a regular (Eulerian) grid. This last step requires the specification of the size of the interpolation area around a grid point. In the case of experiments reported here, the Digimage grid spacing was taken to be 1 cm in both the x and y directions. This value is of the same order of magnitude as the length scale of the Lagrangian measurement averaging, which was set at 2 cm (with a linearly decaying weight function). While smaller length scales are present in the physical flow, the particle-tracking velocimetry as implemented here retains information only about changes in velocities over length scales larger than ~ 1 cm.

Stationary “reference lights” in the field of view of the video camera were used to provide a better Digimage tracking capability and a time reference for the video records. Light-emitting diodes were actually lit according to a signal derived from the PC controlling the rotation rate of the table. With these accurate temporal references, Digimage can be used to begin the tracking of particles at well-defined positions on the videotape; “instantaneous” velocity fields are then computed using a time-averaging window of 1 s.

b. Numerical experiments

The numerical model Gaia was used to simulate the laboratory experiments at laboratory scales. Gaia is a primitive-equation hydrodynamic/transport model in generalized x - y but level z coordinates. The model equation set contains momentum equations in hydrostatic form and conservation equations for mass, heat, salinity S , and other tracers. The equation of state is typically taken from UNESCO (1981), but for these calculations the equation of state previously expressed was used.

Equations are solved by finite differences on a staggered grid: pressure and density variables are cell centered and velocities are determined on appropriate cell faces (the C grid). The upper fluid surface is free. Momentum equations are solved in flux conservation form (Williams 1969; Arakawa and Lamb 1977) using the pressure solution method of Harlow and Welch (1965) in implicit form as discussed by Dukowicz and Smith (1994). The underlying generalized elliptic equation is solved by the multigrid method (e.g., Briggs 1987). Time stepping is by leapfrog (e.g., Wang and Ikeda 1997) and the computational mode is suppressed with an Asselin (1972) filter ($\alpha = 0.01$). Equations for S , temperature, and other tracers are upstream differenced and then corrected for numerical diffusion using the method of Smolarkiewicz and Clarke (1986). In the present application, S is the only intrinsic variable that needs to be time integrated.

Because of the time-variable Ω , the horizontal momentum equations take the following slightly atypical form:

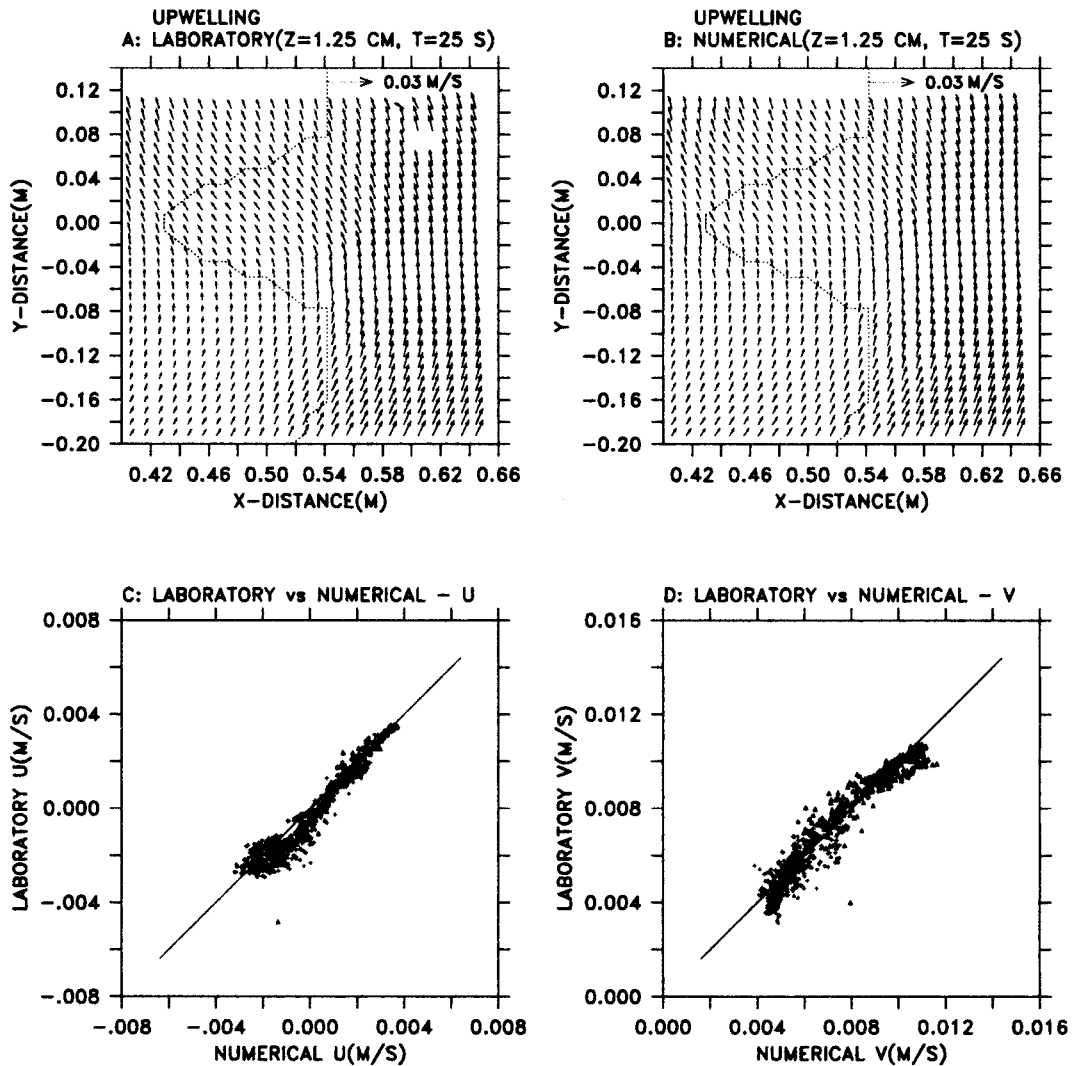


FIG. 4. Laboratory data and numerical results comparison: horizontal velocity field at $z = z_1$ (i.e., above the shelf level; see Fig. 2b) and $t = 25$ s (one rotation period) after the start of the upwelling favorable forcing: (a) laboratory data; (b) numerical results; (c) correlation plot for the cross-shore (u) component of the velocity, where each point corresponds to a given spatial location and the ordinate (abscissa) is given by the laboratory (numerical) value (the ideally good agreement being materialized by the dashed $x = y$ line); and (d) same as in (c) but for the v (alongshore) component of the velocity.

$$\begin{aligned} \frac{D\mathbf{v}}{Dt} + 2\boldsymbol{\Omega} \times \mathbf{v} \\ = -\frac{\nabla p}{\rho_0} - \frac{d\boldsymbol{\Omega}}{dt} \times \mathbf{r} - \boldsymbol{\Omega} \times \boldsymbol{\Omega} \times \mathbf{r} + \mathbf{F}_{\text{Diss}}, \end{aligned} \quad (5)$$

where D/Dt is the material derivative, \mathbf{v} is the horizontal velocity vector, t is the time, p is the pressure, ρ_0 is a reference density, \mathbf{r} is the radius vector with origin at the center of the turntable, \mathbf{F}_{Diss} represents dissipative forces, and $\boldsymbol{\Omega}$ is the time-variable rotation rate vector aligned in the positive z (upward) direction. The second and third (centripetal) terms on the right and the Coriolis term on the left all arise from the transformation of the

equations of motion from a fixed to a rotating coordinate frame. Aspects of this equation that are not associated with oceanic models are (i) the term involving $d\boldsymbol{\Omega}/dt$, (ii) the fact that $\boldsymbol{\Omega}$ is time dependent in the Coriolis force, and (iii) a (time dependent) centripetal term that is usually subsumed into the definition of sea surface in ocean models. The forcing associated with these non-oceanic terms can be rephrased in terms of body forces. Their form, when expressed in terms of $\boldsymbol{\Omega}(t)$ or $\boldsymbol{\Omega}(t) - \boldsymbol{\Omega}_0 = \boldsymbol{\omega}(t)$, is identical for both oscillatory changes in rotation rate (Boyer et al. 2000) and for the “impulsive” forcing considered here.

In order to discuss the impulsive nature of the forcing,

let us write Eq. (5) in cylindrical coordinates (neglecting viscous effects):

$$\frac{\partial v_r}{\partial t} + (\mathbf{v} \cdot \nabla)v_r - \frac{v_\theta^2}{r} - 2\Omega(t)v_\theta = -\frac{1}{\rho_0} \frac{\partial p'}{\partial r} + F_r$$

$$\frac{\partial v_\theta}{\partial t} + (\mathbf{v} \cdot \nabla)v_\theta + \frac{v_r v_\theta}{r} + 2\Omega(t)v_r = -\frac{1}{\rho_0 r} \frac{\partial p'}{\partial \theta} + F_\theta, \quad (6)$$

with

$$F_r = 2\Omega_0\omega(t)r + [\omega(t)]^2 r \quad F_\theta = -\frac{d\omega}{dt}r, \quad (7)$$

where v_r and v_θ are the radial and azimuthal components of the horizontal velocity; Ω_0 is the rotation rate prior to the (impulsive) change; p' is the pressure perturbation from the pressure p_0 , which prevails under centrifugal equilibrium at rotation rate Ω_0 ; $\omega(t)$ is the function of time that describes the change of rotation rate $\Omega(t) = \Omega_0 + \omega(t)$; r is the distance from the center of the turntable; and finally F_r and F_θ are forcing terms corresponding to the fact that the rotation rate of the reference frame is changing. The label “forcing terms” refers to the fact that these terms are not proportional to the relative velocity of the fluid; other terms also vary due to the rotation rate change, that is, the Coriolis “force.”

Initially ($t < 0$), while the rotation rate is constant ($\Omega = \Omega_0$), F_r and F_θ are zero. When $t > \Delta t$, the time interval over which the rotation rate is changed, the rotation rate is constant ($\Omega = \Omega_1$) and consequently F_θ is again zero. The alongshore forcing term F_θ is thus exerted over a duration Δt , which is 1 s in our experiments. In addition, F_r is nonzero for all $t > 0$, but its value is constant for $t > \Delta t$. In the absence of a canyon and if the fluid was indeed nonviscous, a simple solution at $t > \Delta t$ would be $v_r = 0 = p'$, $v_\theta = -(\Omega_1 - \Omega_0)r = -(\Delta\Omega)r$: a purely azimuthal flow would be forced. Nonetheless, at large t , owing to viscous effect, the fluid eventually adjusts and the motion takes the form of a solid-body rotation at the new rotation rate Ω_1 . Velocity in the tank is then reduced to zero and hence the pressure will adjust itself in order to compensate the “differential centrifugal force”:

$$-\frac{1}{\rho_0} \frac{\partial p'}{\partial r} = -F_r(t > \Delta t) = -([\Omega_1]^2 - [\Omega_0]^2)r, \quad (8)$$

where p' is the difference between initial and final state pressures. After viscous adjustment, the difference between initial and final states is just the change of the parabolic shape of the isopycnals and fluid surface due to the new centrifugal force.

As with laboratory experiments, the principal numerical experiments began with the tank rotating at $\Omega_0 = (0.269, 0.232) \text{ s}^{-1}$ for upwelling and downwelling studies, respectively, and these rates were changed linearly over $\Delta t = 1 \text{ s}$ to reach a common Ω_1 value of 0.251 s^{-1} . A parameter study of effects of bottom fric-

tion (section 3a) and the extension of results to a slower change of rotation rate (section 3b) were performed using a slightly different upwelling favorable configuration: $\Omega_0 = 0.251 \text{ s}^{-1}$, $\Omega_1 = 0.232 \text{ s}^{-1}$.

As is well known, hydrodynamic model results depend crucially on the subgrid-scale parameterizations. Because tank motions appeared to be laminar or near laminar, viscosity and horizontal salt diffusion coefficients in the fluid interior were given molecular viscosity magnitudes (i.e., $10^{-6} \text{ m}^2 \text{ s}^{-1}$); vertical salt diffusivity was set to zero. Setting vertical diffusivity equal to zero prevented the evolution of the density profile in the absence of fluid motion. Numerical experiments were also undertaken with viscosity/diffusion coefficients 10 times larger than molecular levels.

Boundary conditions in the numerical model were such that normal flow was always zero. Shear stress along the free surface and on all side surfaces was set to zero. At the tank floor, a shear condition was used to impart the effects of bottom friction on the flow. Bottom friction dissipation is important because the laboratory flow had been observed to slow more quickly on the shelf than in the deeper parts of the tank, meaning that the energy loss was not entirely by dissipation within the fluid interior.

Shear stress at the bottom τ_D is often given in the form $\tau_D = \rho_0 C_D \mathbf{v}|\mathbf{v}|$, where ρ_0 is fluid density (998 kg m^{-3}), C_D is a drag coefficient, and \mathbf{v} is velocity value in the free stream above the bottom. Bottom stress is also equal to $[A_Z dv/dz]_{z=-h}$, where h denotes bottom depth. Most often the two forms of stress are equated and then, after assigning values to C_D and $[A_Z]_{z=-h}$, they are used to determine $[dv/dz]_{z=-h}$. The approach in Gaia is different in that the equivalence of the two stress forms is used to determine $[A_Z]_{z=-h}$, having fixed $[dv/dz]_{z=-h}$ by requiring that $[v]_{z=-h} = 0$. If bottom stress in quadratic form τ_D is evaluated at a height of one-half a computational cell above tank bottom, then one can show that $[A_Z]_{z=-h} = C_D |v| dz/2 + \nu$, where ν represents molecular viscosity ($10^{-6} \text{ m}^2 \text{ s}^{-1}$), and $|v|$ is the total fluid speed at that level. For each computational column and time step, viscosity on the tank bottom $[A_Z]_{z=-h}$ is adjusted so that the value of $[A_Z dv/dz]_{z=-h}$ is consistent with the value of τ_D given in quadratic form and with a condition of zero horizontal flow at $z = -h$. For $|v|$ typically $\sim 1 \text{ cm s}^{-1}$ and $dz = 5 \text{ mm}$, C_D values of 10^{-3} , 0.04, and 1.0 lead to $[A_Z]_{z=-h}$ values of ν , 2ν , and 26ν , respectively. The best values of C_D and interior mixing coefficients were determined empirically through comparisons of numerical with laboratory data, as discussed below.

Boundary conditions for S prevented gradients at the tank surface or bottom. Lateral boundary conditions on velocities and S were not needed, because the horizontal mixing coefficients were deliberately set to zero on the walls of the model tank. Setting mixing to zero along horizontal boundaries ameliorates the bookkeeping of virtual values for variables in regions of nonuniform

bathymetry. Since the wetted surface in the tank is primarily the bottom surface rather than side surfaces, skirting the issue of friction effects at tank sidewalls should have only a modest effect on results.

Initially the fluid in the tank was in solid-body rotation. The primary balance in that case is between centrifugal forces and radial pressure gradients arising from the parabolic level of the fluid surface. An analytic solution to that balance equation determined the solid-body surface height. Preliminary model experiments initialized with that free surface and with level isopycnals, when run to 4000 time steps, showed no drift from that initial state in the absence of additional forcing. No model spinup to initial steady state was thus required.

The initial density profile was adopted from measurements (Fig. 2). Isopycnals were made level at the start of the forcing, though they more likely are slightly bowed upward with increasing radius as the result of rotation. Since differences in actual surface levels between R_1 and R_4 amount to only 2 mm, the neglect of bowing of isopycnals in the initialization of the model is not considered an encumbrance to obtaining accurate results. The alternative is to use the geopotential surface as the reference level, but that is not the reference level used in the laboratory.

Numerical solutions were computed on rectangular grids with ranges of indices $(N_x, N_y, N_z) = (128, 128, 25)$. Cell size was uniformly $1.4 \times 1.4 \times 0.5$ cm³. A few additional experiments were performed at higher resolution. With the given cell height, the numerical model could not resolve details of the bottom boundary Ekman layer; the height of the (laminar) Ekman layer scales as $(2\nu/f)^{1/2} = 2$ mm when ν is the kinematic viscosity and when f , as in these experiments, is ~ 0.5 s⁻¹. Despite this, the bulk effects of bottom friction on circulation were well represented, as will be demonstrated in the following sections.

The numerical model time step Δt was ~ 28 ms, approximately twice that of the Courant–Frederichs–Lewy (CFL) stability condition for surface gravity waves in the tank. Had explicit numerical procedures for time advancing of free surface η been used (e.g., PHB), the stability constraint would have demanded smaller time steps. Computations were performed on a single processor Digital Equipment Alpha workstation running at 600 MHz and required approximately 12.3 h of CPU time for each simulation of 150 s.

3. Laboratory and numerical comparisons

a. Bottom friction

Bottom friction is important in controlling circulation in the tank. As a comparison of Figs. 4a and 5a indicates, laboratory velocity fields obtained at a depth of 1.25 cm during an upwelling experiment at $t = 25$ and 100 s (corresponding to 2 and 8 pendulum days after initiating the forcing) are much different. Slowing of laminar

tank flow is a frictional effect, and that effect is first evident on the shelf. Figure 4a shows that at $t = 25$ s the flow in the upper layers is deflected above the canyon and on the shelf (downstream of the canyon). Nevertheless, the fluid is basically able to flow across the canyon, which is an effect of the density stratification (if the fluid was homogeneous, the strong perturbation induced by the canyon at lower levels, see section 3b, would also be observed above the shelf level). Later, at $t = 100$ s (Fig. 5a), the flow over the shelf is seen to have been strongly decelerated, now having only $\sim 20\%$ of the peak speed. Over the model continental slope at the same depth, the fluid has barely spun down ($\sim 95\%$ of peak speed). For the weakly stratified shelf (Fig. 2), the barotropic spindown time, $(2h^2)^{1/2}/\nu f$, is 50 s, much like the timescale observed for shelf fluid. Though the water everywhere in the tank will ultimately adjust to a new solid-body rotation state without motion relative to the bathymetry, the rapid slowing of motion above the shallow shelf is an important clue to bottom frictional strength.

To assess the similarity of results, the laboratory data (Figs. 4a and 5a) were compared to corresponding numerical data (Figs. 4b and 5b) at the same time and level. Figures 4c and 4d and 5c and 5d are correlation plots of laboratory and numerical results for cross-shore (panels C) and alongshore (panels D) velocities at respective times. The abscissa (ordinate) of each point in Fig. 4c, for example, is the numerical (laboratory) u values for all points sampled at the depth and time indicated. The solid line in Figs. 4c, 5c and 4d, 5d represents an ideal distribution of perfect correlation between laboratory and numerical model values. With actual points lying close to the $x = y$ line, these scatter diagrams suggest little systematic error in numerical results, or in the implementation of the physical experiments. The striking agreement exhibited in Figs. 4 and 5 was not serendipitous; they result from choices made after conducting experiments on the sensitivity of correlations to values of bottom friction (C_D) and interior mixing (ν) values in the numerical model, as is explained below.

Figure 6 shows analogous correlation plots of v velocity for four numerical experiments, all for $t = 100$ s, with differing bottom drag (C_D) or interior mixing coefficient (ν). Figure 6a represents a free-slip bottom velocity boundary condition, that is, $A_z[z = -h] = 0$; Fig. 6b is the best choice set with $\nu = 0.01$ cm² s⁻¹ and $C_D = 3 \times 10^{-3}$; Fig. 6c is a choice of $\nu = 0.01$ cm² s⁻¹ and $C_D = 0.3$; and Fig. 6d represents results for interior mixing and $A_z[z = -h]$ both equal to 10ν . The sequence from Fig. 6a (free-slip bottom condition) to Fig. 6d (large dissipation everywhere) illustrates the importance of the values for bottom drag and interior mixing. Points below the perfect correlation line in Fig. 6a indicate that numerical model velocities are larger than laboratory ones, which is one result of an insufficiently large bottom drag. In contrast, points above the

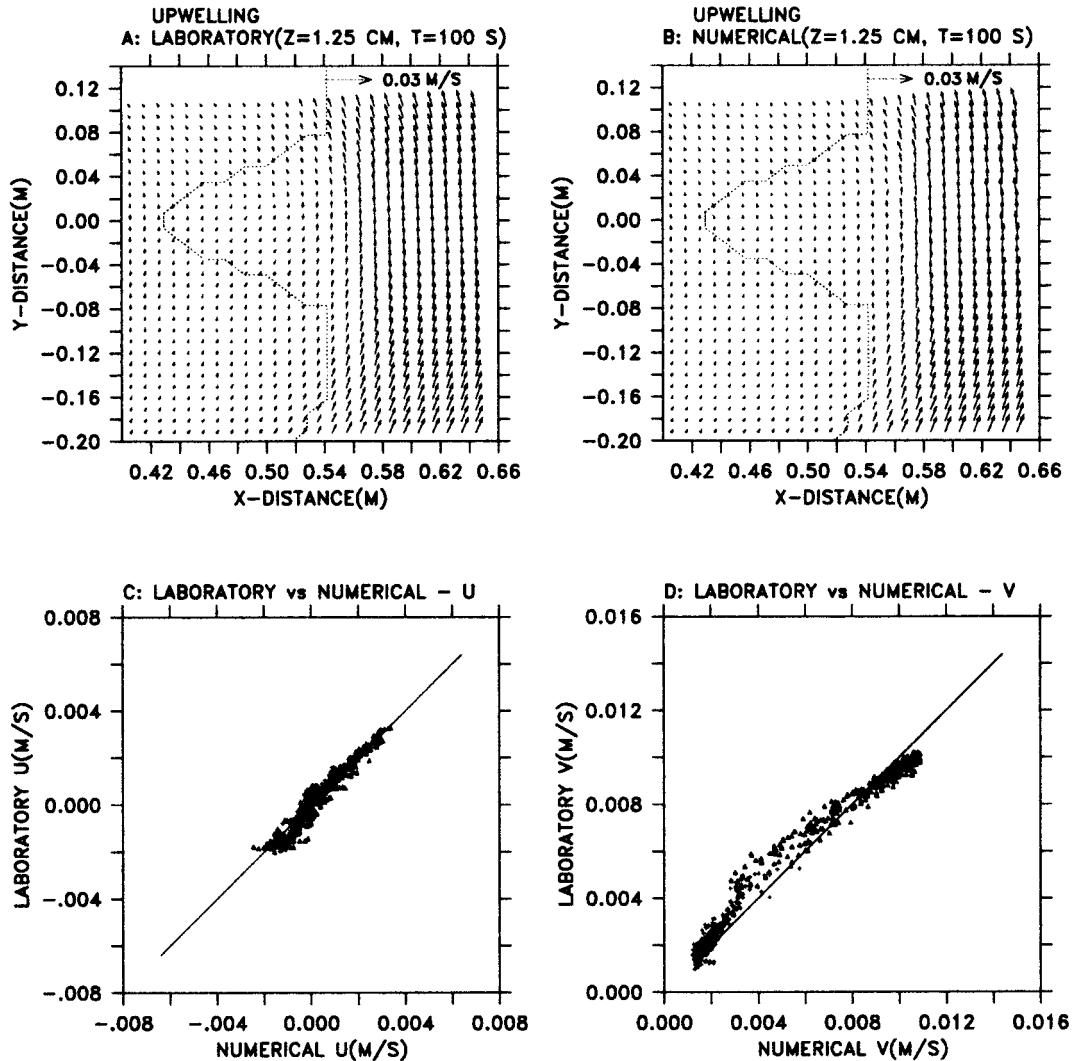


FIG. 5. Same as in Fig. 4 but for time $t = 100$ s.

perfect correlation line in Fig. 6d represent numerical model velocities that are smaller than their laboratory counterparts, due to excessive interior dissipation and bottom drag. Smaller velocities in all diagrams, that is points closest to the origin in correlation plots, typically correspond to shelf values, and largest velocities typically are for flow over greatest tank depths. In the first (Fig. 6a) and last (Fig. 6d) cases, the error is clearly systematic. Neither a free-slip bottom boundary condition nor an interior fluid viscosity larger than molecular level is appropriate (note that the numerical model Gaia is actually able to cope with molecular ν in these experiments). It is clear that care must be taken with assigning bottom boundary conditions and interior mixing values.

The best correlation (Fig. 6b) is obtained with a molecular value ν for interior mixing and for $A_z[Z = -h] \sim \nu$ ($C_D = 3 \times 10^{-3}$) as well. Results are poorer (Fig. 6c) when $A_z[Z = -h]$ is merely increased to 8.5ν (C_D

$= 0.3$). The condition $A_z[Z = -h] < 1.1\nu$ is obtained, for an above-bottom laboratory velocity $|v|$ of 1 cm s^{-1} and a $dz = 5 \text{ mm}$, when $C_D < 4 \times 10^{-3}$. We have used the value $C_D = 3 \times 10^{-3}$ in Fig. 6b and all subsequent calculations, when essentially any value less than $< 4 \times 10^{-3}$ would do, only because that value is typical of the drag coefficient in real atmospheric and oceanic flows. At those scales, both $|v|$ and the distance above the bottom to the free-stream level, here represented by dz , would be much larger. Thus in the actual ocean, $A_z[Z = -h] \gg \nu$ as are mixing coefficients in the interior.

Having found that the best agreement between the laboratory and numerical experiments occurred with a molecular value for interior mixing coefficients and with a bottom drag coefficient $C_D < 4 \times 10^{-3}$, we left the dissipation scheme unchanged in all subsequent numerical experiments. In effect the observed spindown rate observed in laboratory measurements was first used

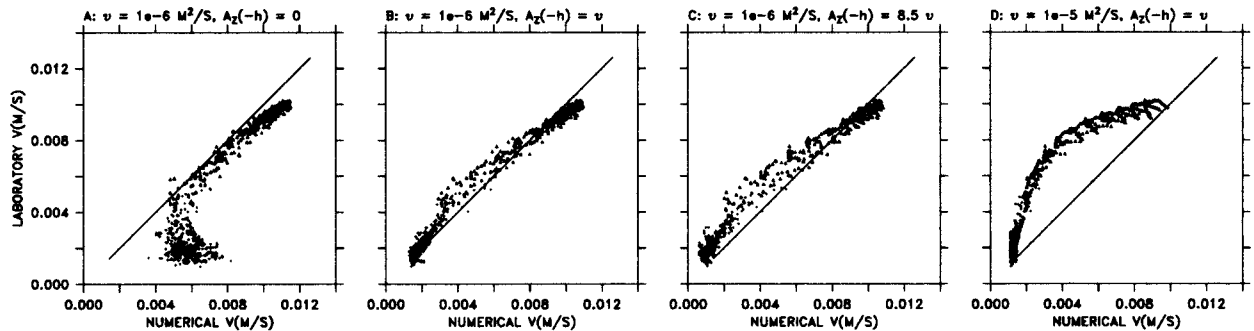


FIG. 6. Sensitivity of numerical results to bottom drag and internal mixing parameterizations for the upwelling experiment. (a) Correlation plot of the alongshore (v) component of the velocity at $t = 100$ s for the upper level ($z = z_1$, see Fig. 2b) with $A_z[z = -h] = 0$ (see text, section 3b); (b), (c), and (d) $C_D = 3 \times 10^{-3}$, $\nu = 0.01 \text{ cm s}^{-2}$; $C_D = 0.3$, $\nu = 0.01 \text{ cm s}^{-2}$; and $C_D = 3 \times 10^{-3}$, $\nu = 0.1 \text{ cm s}^{-2}$, respectively.

to “calibrate” the dissipation coefficients in the numerical model. We will now see that interesting dynamics occur within the canyon before the flow has been dissipated on the model continental shelf and well before it has been substantially slowed down in deeper areas.

b. Flow behavior

1) TEMPORAL EVOLUTION AT THE SHELF-BREAK LEVEL FOR THE UPWELLING FAVORABLE FORCING

In actuality, adjustments to the rotation rate change occur over three different timescales: first, along canyon surges; second, vortex development and advection to midcanyon occurring within typically 2–3 rotation periods; then slow decay of the canyon vortex over 5–10 rotation periods. Later still currents in the entire test tank are reduced to zero: at that point the fluid will have finally been accelerated to solid-body rotation at the new rotation rate.

In the upwelling case, the initial response of the system is to force upcanyon flow (Figs. 7a,b). Note that numerical results are given at a level that is slightly deeper than that of the shelf, the nominal center-plane depth of the light sheet used in our laboratory experiments. Numerical results indicate that midway along the canyon ($x = 0.55$ m), the maximum upcanyon velocity (1.2 cm s^{-1}) occurs at $t = 3$ s and is centered on the upstream canyon wall at a depth of 4 cm. Some downcanyon flow is also observed at the same time, but its maximum value is only $\sim 4 \text{ mm s}^{-1}$. This primarily upwelling response can be interpreted using the argument developed in Freeland and Denman (1982) because an analogy exists between our forcing and the oceanic forcing realized by a large-scale (compared to the canyon dimensions) geostrophic current. At times larger than $t = 1$ s (when the rotation rate is again constant), far from the canyon (so that $\partial/\partial\theta \equiv 0$ and $v_r = 0$), and in the absence of dissipation, the radial force balance in Eqs. (6) and (7) is

$$2(\Omega_1)v_\theta + r\Delta(\Omega^2) + \frac{v_\theta^2}{r} = 0, \quad (9)$$

where $v_\theta = -(\Delta\Omega)r$ and $\Delta(\Omega^2) = (\Omega_1)^2 - (\Omega_0)^2$; the balance in the radial direction is trivial since all terms are zero. Note that this is simply the balance satisfied by the azimuthal flow already discussed in section 2b: in particular, it is assumed that p' is still zero, meaning that t is not large enough for frictional effects to have significantly spun up the fluid to its new solid-body rotation. The first term is the Coriolis force, the second is the “differential centrifugal force” (due to the change of rotation rate), and the third term is the centrifugal force due to the relative velocity of the fluid in the cylindrical geometry. Compared to the first two terms, the third term is negligible. Thus equilibrium is an approximate balance of Coriolis and differential centrifugal forces. Note that the differential centrifugal force is a function of r only and does not depend on the behavior of the flow. This balance, which is expected to hold far from the canyon before viscous effects are able to significantly slow the azimuthal current $v_\theta(r)$, is analogous to that of a geostrophic current, with the geostrophic pressure replacing our differential centrifugal term.

In the case of a decrease of rotation rate (i.e., a flow leaving the coast on its left, i.e., $v_\theta > 0$), the argument developed by Freeland and Denman (1982) on the basis of observational evidence can then explain why the forcing is indeed “upwelling favorable,”¹ as clearly shown by Fig. 7. This mechanism can be applied to our experiments as follows: far from the canyon and before the fluid has been accelerated to the new rotation rate, the differential centrifugal force and the Coriolis force acting on the azimuthal velocity v_θ are in approximate equilibrium. Over the canyon the same hold true. In the canyon itself alongshore flow cannot be as large. Con-

¹ The upwelling direction is thus the same as for the upwelling induced by the flux of the Ekman layer; the canyon upwelling mechanism, however, does not ultimately rely on bottom friction.

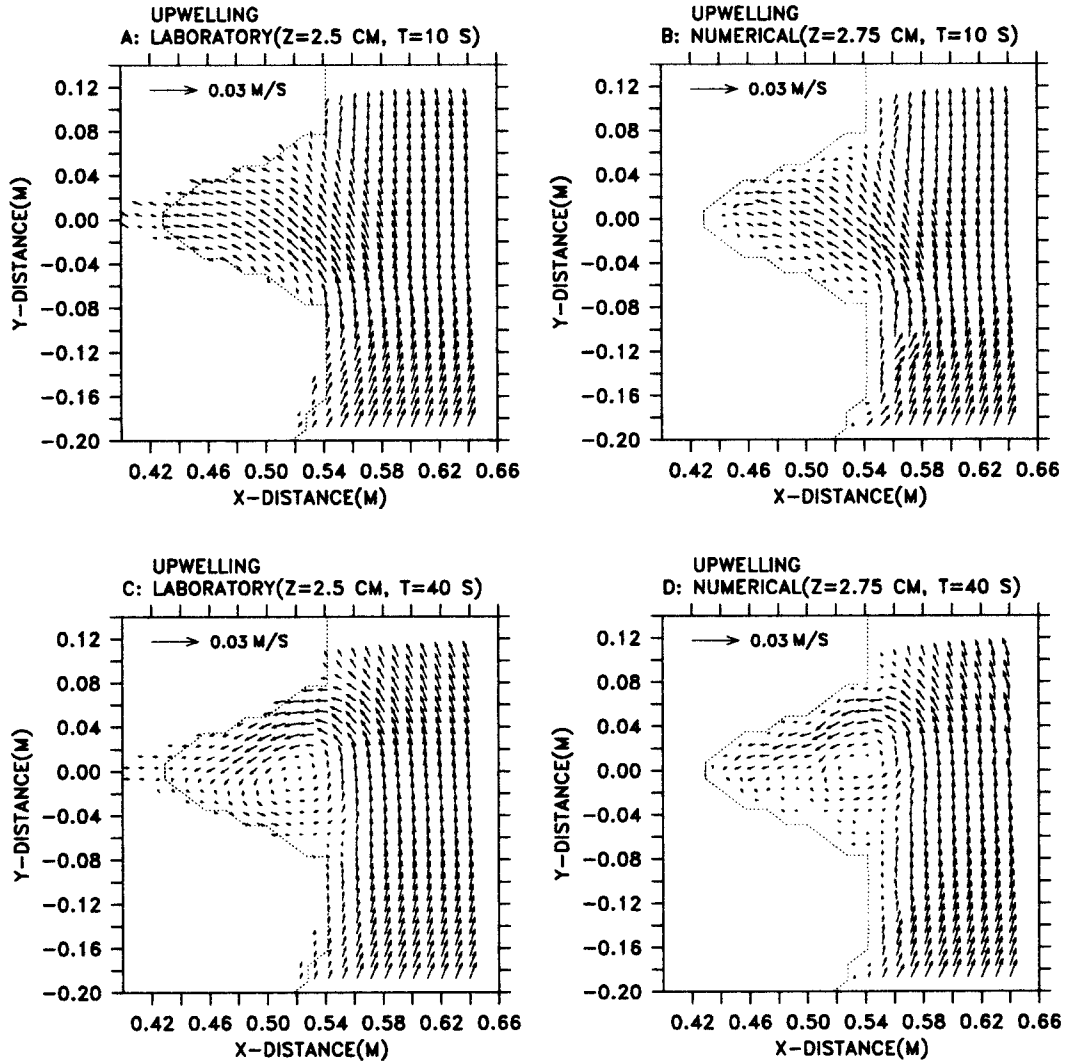


FIG. 7. Laboratory and numerical velocity fields during the upwelling experiment, at the shelf-break level. (a) and (b) The model time is $t = 10$ s, corresponding to 14 h in the ocean at a latitude where $f = 10^{-4} \text{ s}^{-1}$; (c) and (d) $t = 40$ s. The laboratory data are shown in (a) and (c), the numerical results in (b) and (d).

sequently, the radial component of the Coriolis force cannot balance the prevailing differential centrifugal force within the canyon, and this imbalance then accelerates an onshore flow (if the forcing is upwelling favorable, of course).

One must recall that the Freeland and Denman (1982) argument neglects variations across the canyon and, thus, is more appropriate for thin canyons ($W/L \ll 1$). The model employed here is characterized by $W/L = 1.3$: in such conditions it is not surprising to observe that velocity gradients develop across the canyon (see below), thereby limiting the validity of the simple interpretation to small time increments. As mentioned earlier, a typical submarine canyon would have $W/L < 1$, but W/L is, of course, never infinitesimal. Additional experiments have been conducted to investigate the nature of the upwelling when topography is characterized

by $W/L = 0.67$. Results of those experiments did show that the uniform upwelling holds for a longer time in a thin canyon than in a wider canyon, all other nondimensional parameters being kept constant (not shown). Another effect that is not taken into account by the canyon upwelling mechanism of Freeland and Denman (1982) is the possibility of developing baroclinic pressure gradients, which might inhibit or change the nature of the subsequent upwelling.

The experiments show that the primarily upcanyon flow does not hold for a long time: a cyclonic eddy is seen in the canyon approximately one rotation period after the initiation of the experiment and reaches the state depicted by Figs. 7c and 7d at $t = 40$ s. This eddy then dissipates relatively slowly: it is still clearly observed at $t = 100$ s (i.e., after four rotation periods, not shown).

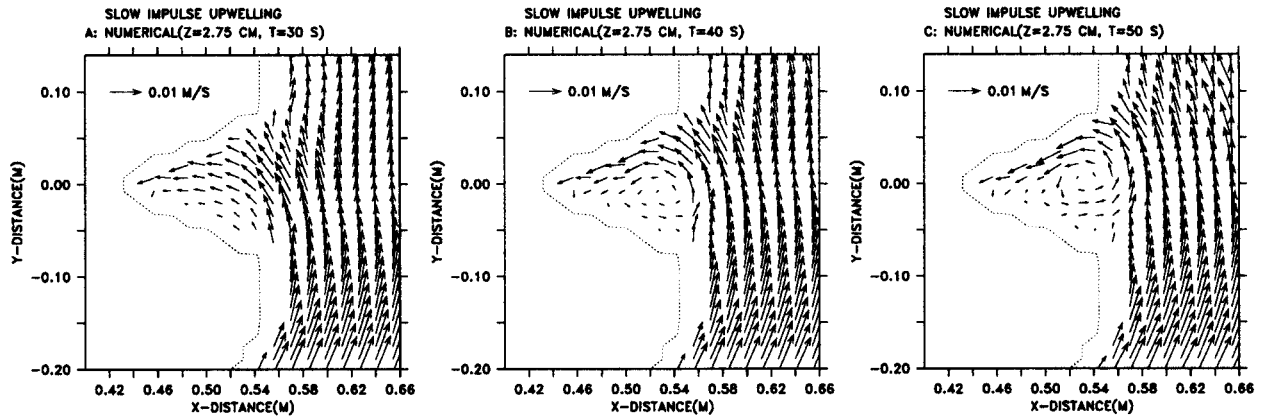


FIG. 8. Influence of rotation rate change on velocity fields during the upwelling experiment, at the shelf-break level. (a), (b), and (c) The numerical velocity fields obtained at $t = 30$, 40, and 50 s with a slower rotation rate change ($\Delta t = 25$ s).

The generation of the cyclonic eddy could be imputed to the suddenness of the change of rotation rate used to force the flow. Experiments in which the rate of rotation changed over times longer than 1 s were not run in the laboratory, but Fig. 8 shows some numerical results in a case where the change of rotation rate was applied over a period of 25 s (one rotation period or 2 pendulum days). Although the transient evolution is, of course, different (for instance, cf. Fig. 8b to Fig. 7d), Fig. 8 shows that the cyclone is not simply a “starting eddy” whose very existence would be dependent on the initial temporal evolution of the forcing. The cyclone is generated although the rotation rate change is much more progressive.

Several mechanisms can be advanced to account for the vorticity generation inside the canyon. First, one can consider the natural tendency of the flow to detach from the sloping region. Recall that the topography considered here has a small scale compared to the internal radius of deformation (high Burger number), which is the spatial scale upon which the flow is able to adjust geostrophically (and thus to follow isobaths). One can also note that the criterion according to which an alongslope flow should not separate by inertia if the inertial radius U/f is smaller than the isobath radius of curvature (e.g., Bormans and Garrett 1989) is only marginally satisfied at the canyon “corners.” In order to explain observed vorticities, one can invoke (at least) two other mechanisms, based upon the stretching of planetary vorticity. There is the inertial tendency for shelf water masses to flow over the canyon rim: this would lead to some amount of stretching at the canyon rim level, hence the generation of positive (cyclonic) vorticity, whether the forcing is upwelling or downwelling favorable. Finally in deeper layers (inside the canyon), one can consider the stretching that would occur in upwelling conditions (Klinck 1996), if the upwelling is intensified at the canyon rim and gets weaker as depth increases. The latter mechanism was

actually found to explain the order of magnitude of the cyclonic vorticity found below the canyon rim by Hickey (1997). Finally, one can add the fact that if an offshore-directed countercurrent develops [with respect to the tendency given by the Freeland and Denman (1982) mechanism], it can be accelerated by baroclinic pressure effects: for instance in the upwelling case, deeper (heavier) water masses are piled upon the canyon head, giving rise to a restoring pressure force directed against the upwelling tendency. We will thus consider here three basic mechanisms, that might generate vertical vorticity in the canyon area: (i) slope flow detachment, (ii) canyon rim stretching, and (iii) deep upwelling stretching (or deep downwelling squashing). Returning to the cyclonic vorticity that is observed at the rim level under upwelling favorable forcing, we will argue it is due to a combination of effects i and ii, which in this case are acting in the same cyclonic sense.

2) SYMMETRY OF THE FLOW RESPONSE WITH RESPECT TO THE FORCING DIRECTION

In its evolution from an initially uniformly upwelling or downwelling state, the flow behavior, at the shelf-break level, exhibited asymmetry with respect to the forcing direction. This asymmetry, however, was observed to decrease with depth.

At the shelf-break level, one would expect, by symmetry, the generation of an anticyclonic eddy by downwelling favorable forcing, since a cyclonic eddy was observed for upwelling favorable forcing. Nonetheless, this is clearly not the case, as shown by Fig. 9. First note that an asymmetric behavior already takes place during the initial response: the flow is not so clearly downwelling in Figs. 9a and 9b, as it is upwelling in Figs. 7a and 7b. Such an asymmetry is reminiscent of results presented in Klinck (1996). Second, no eddy at this depth is formed at a later stage (cf. Figs. 9c,d and Figs. 7c,d), indicating that the flow behavior is highly

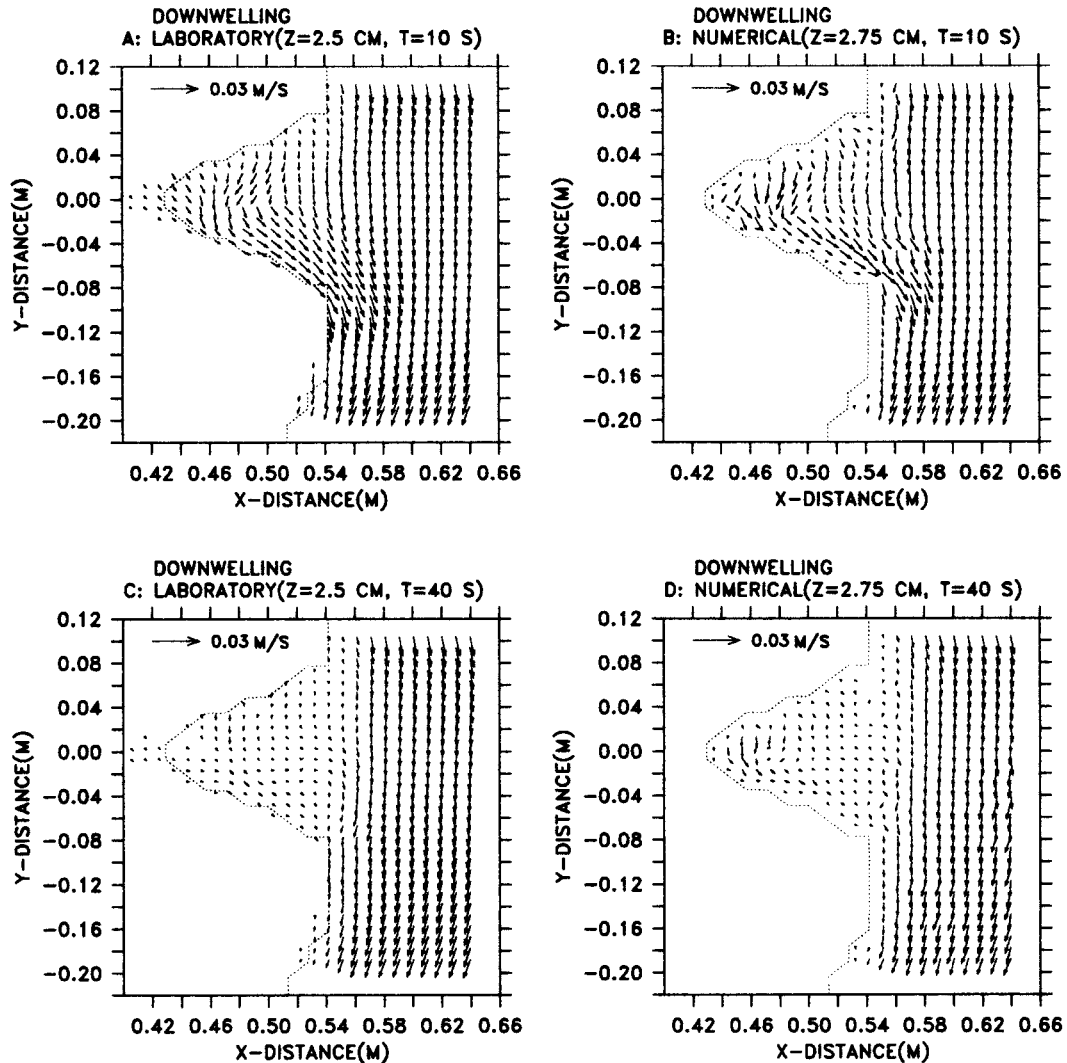


FIG. 9. Laboratory and numerical velocity fields during the downwelling experiment, at the shelf-break level. The display parallels that of Fig. 7 for the upwelling case.

asymmetrical at the shelf-break level. On the contrary, the flow response appears to be much more symmetric at the lower ($z = z_3$) level: again, a cyclonic eddy appears in the upwelling favorable experiment (Figs. 10a,b), but now one can also see a corresponding anticyclonic eddy in the downwelling favorable experiment (Figs. 10c,d). Weak asymmetries can nevertheless be noticed, concerning the strength and position of these eddies.

The vertical extent of the (anti-) cyclonic eddy that occurs inside the canyon under (down-) upwelling favorable forcing is further documented in Fig. 11, which shows along-axis sections of vertical relative vorticity, $(\partial v/\partial x) - (\partial u/\partial y)$, for both upwelling and downwelling cases at $t = 25$ s. The vorticity generated by the response of flow to topography is not small compared to the background rotation $f = 0.5 \text{ s}^{-1}$. The vorticity extrema

in the respective cases (Fig. 11) have comparable magnitudes, $+0.53 \text{ s}^{-1}$ versus -0.43 s^{-1} , but the core of downwelling vortex is deeper. In both cases, the core of the eddy is not vertical but follows the topographic slope, and vorticity of any significant magnitude is confined to below-shelf depths. Nevertheless, the asymmetric behavior, already noted in horizontal flow fields, is also clearly seen in Fig. 11. At shelf-break depth the vorticity magnitude in the upwelling case is approximately twice that of the downwelling case, but the two cross sections smoothly join symmetrically opposed values as depth increases (reaching a vorticity of approximately $\pm 0.30 \text{ s}^{-1}$ at $z = 10 \text{ cm}$).

The difference between the shelf-break level and deeper, concerning the degree of asymmetry of the flow behavior under upwelling or downwelling favorable forcing, could be *interpreted* with the vorticity gener-

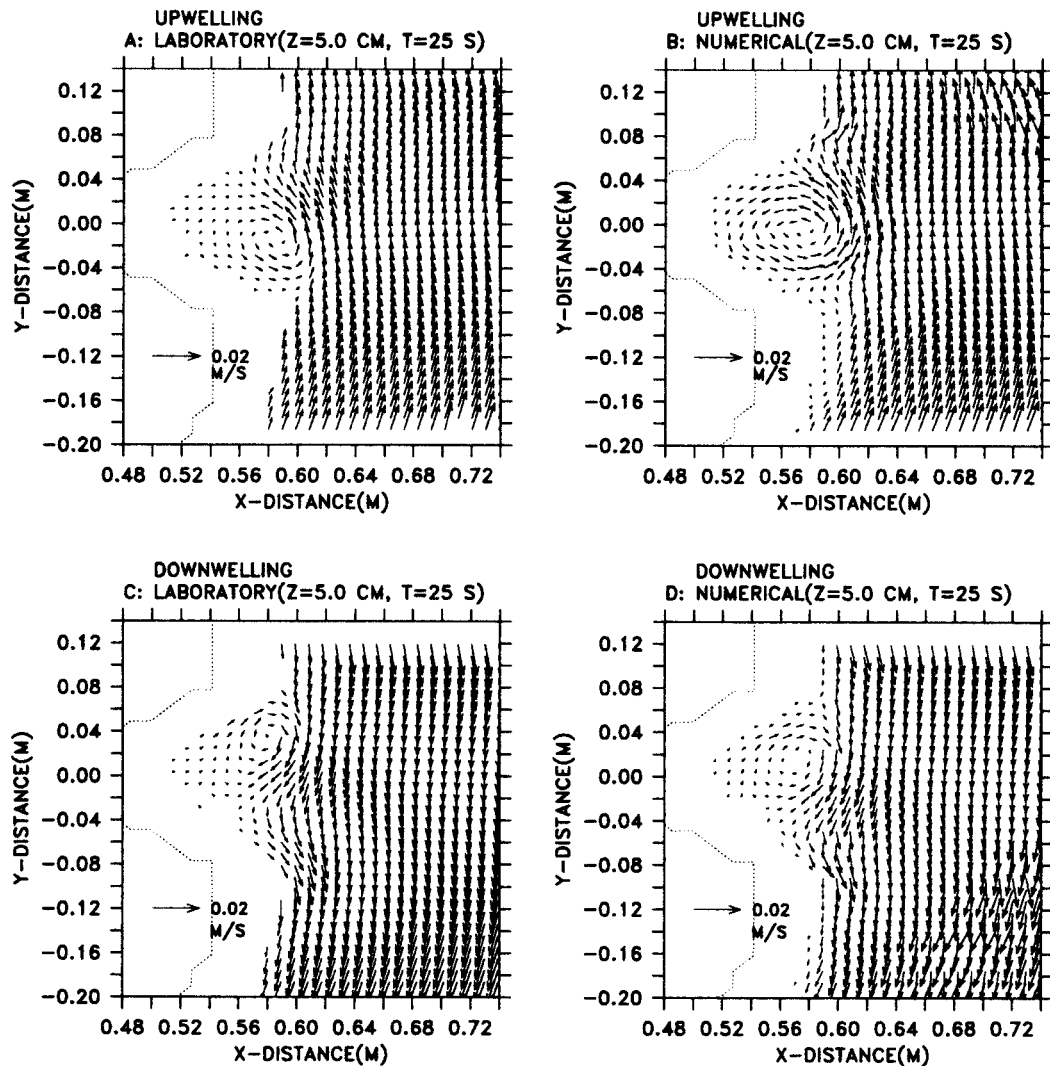


FIG. 10. Laboratory and numerical velocity fields below the shelf break. (a) and (b) An upwelling forcing, and (c) and (d) a downwelling forcing. Model time is $t = 25$ s (one rotation period).

ation mechanisms listed at the end of the previous section. At the shelf-break level, mechanisms i and ii can be invoked; mechanism i, the “slope flow detachment,” leads to cyclonic or anticyclonic vorticity according to the forcing direction whereas mechanism ii, the “canyon rim stretching,” always leads to cyclonic vorticity. These mechanisms act together in the upwelling case but not in the downwelling case, which can provide an explanation for the asymmetry observed at the canyon rim level. Such an interpretation was used in Pérenne et al. (1997) for a barotropic flow, but now flow is stratified and can develop vertical shear in its interior. Consider a situation where layers are moving horizontally and are weakly coupled to each other. Then the main difference between the shelf-break and lower-level layers is that instead of flowing *over* a feature of the bottom topography, the lower layer (e.g., $z = z_3$) is

flowing *along* a lateral boundary. In this simplified view mechanisms i and iii are likely to dominate the vorticity generation below the rim. Since these mechanisms are symmetric with respect to the forcing direction, it is not surprising to observe symmetrically opposed flow patterns in upwelling and downwelling flow conditions below the canyon rim. Anticipating the next section, we mention here that the upwelling of the isopycnals was indeed found to decrease with depth in the laboratory experiments (a condition for mechanism iii, the deep upwelling stretching). The corresponding stretching, however, did not exceed 2 mm, as estimated between levels z_2 and z_3 ; these levels are separated by 25 mm and the observed stretching is thus $\sim 10\%$ of the water column under consideration: this would lead to vorticities of $\sim 0.1f$ and is insufficient to explain measured vorticities ($\sim f$). It seems that in experiments reported

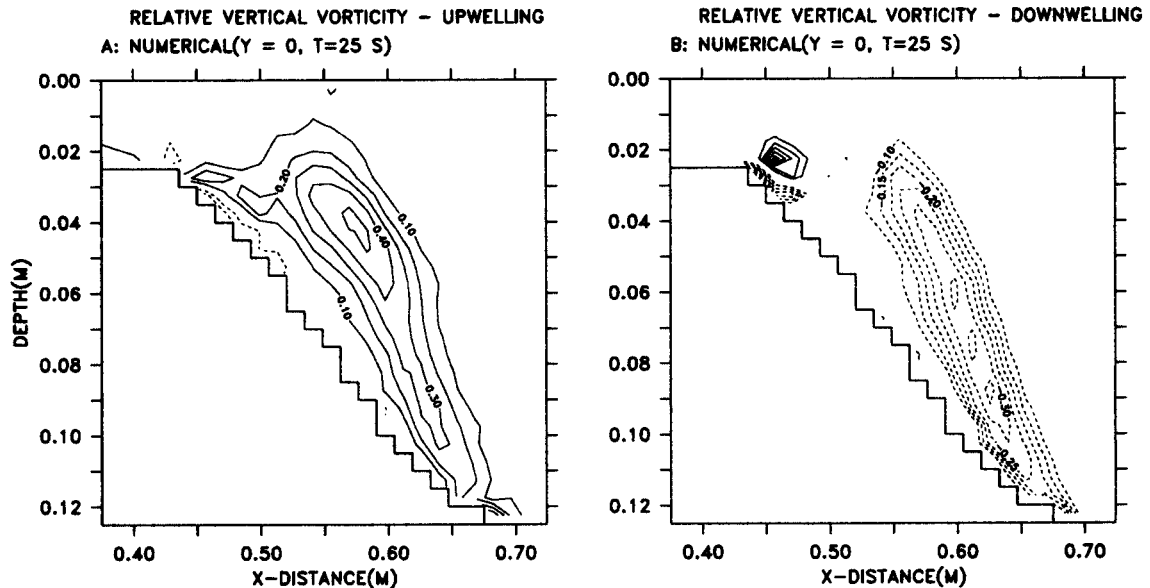


FIG. 11. Vertical section, along the canyon axis, of vertical vorticity at time $t = 30$ s. (a) Upwelling forcing; (b) downwelling forcing. Solid (dashed) lines correspond to positive (negative) values.

here the vorticity generation inside the canyon is mainly due to the slope flow detachment; this conclusion is further supported by the fact that in the laboratory experiments, the (anti-) cyclonic signal at level z_3 originates at the upstream canyon corner and is then advected toward the canyon axis while getting stronger.

That the vortex in midcanyon originates at the canyon boundary is also seen in the numerical results. Figure 12 depicts the time evolution of the vortex at a depth of 5 cm. At $t = 5$ s, vorticity is largest on the upstream side of the canyon near the headland in upwelling and downwelling cases. Subsequently (Fig. 12), the vortex detaches from the canyon wall region and moves into the canyon interior. An animation of vortex stretching (dw/dz) at the same level supports the claim that the midcanyon vortex is not locally generated by upwelling and downwelling along the canyon axis. This result differs from that seen by Klinck (1996) where vortex stretching in the canyon produces cyclones for both upwelling and downwelling cases. The most likely reason for this difference in results is the different ways the flows are forced. In the Klinck (1996) study, for example, the alongshore flow is continually forced in a periodic channel by a constantly maintained offshore boundary condition in the form of a streamfunction.

It must also be stated that the deep stretching mechanism was found to be important for vortex formation in real ocean canyons (e.g., Hickey 1997). That our model generates midcanyon vortices without stretching while stretching seems to be indicted by ocean data may reflect simplifications of natural conditions invoked in our modeling study: barotropic forcing (as opposed to wind stress at the surface) and linear stratification (as

opposed to a pycnocline), both of which should lead to less vertical variability.

3) DENSITY TIME SERIES

We finally consider the density data; some time series of vertical displacement at the shelf-break level are presented in Fig. 13 (upwelling) and Fig. 14 (downwelling). In the upwelling case, the negative surge of probe 1 during the first second (Fig. 13) is in opposite direction to the early evolution at probe 3. That is likely caused by the initial flow at the upstream canyon edge bringing fresher water downward; correspondingly, probe 3 first registers effects of uplifted isopycnals by the side-to-side flow. This could lead to a (small) internal seiche inside the canyon, but larger effects then come into play. There is first a tendency for upward displacement, followed at $t \sim 15$ s (i.e., less than a rotation period) by a downward transient lasting until $t \sim 50$ s (two rotation periods). This transient occurs simultaneously with the development of the cyclonic eddy (Fig. 8). Ultimately, a quasi-steady upward displacement is observed, as expected under upwelling favorable forcing. Some oscillations of period T_R are found: they are due to the (slight) misalignment of the rotation axis with the gravity vector. At the locations investigated, the ultimate upwelling displacement is quite small, only ~ 3 mm in the laboratory, at the shelf level and for the probe locations considered (see Fig. 2b). According to scaling arguments (the details of which can be found in PHB), this amounts only to ~ 15 m at oceanic scales. Numerical results (Fig. 13a) mirror laboratory results (Fig. 13b) in qualitative fashion (including the downward motion at probe 3 during

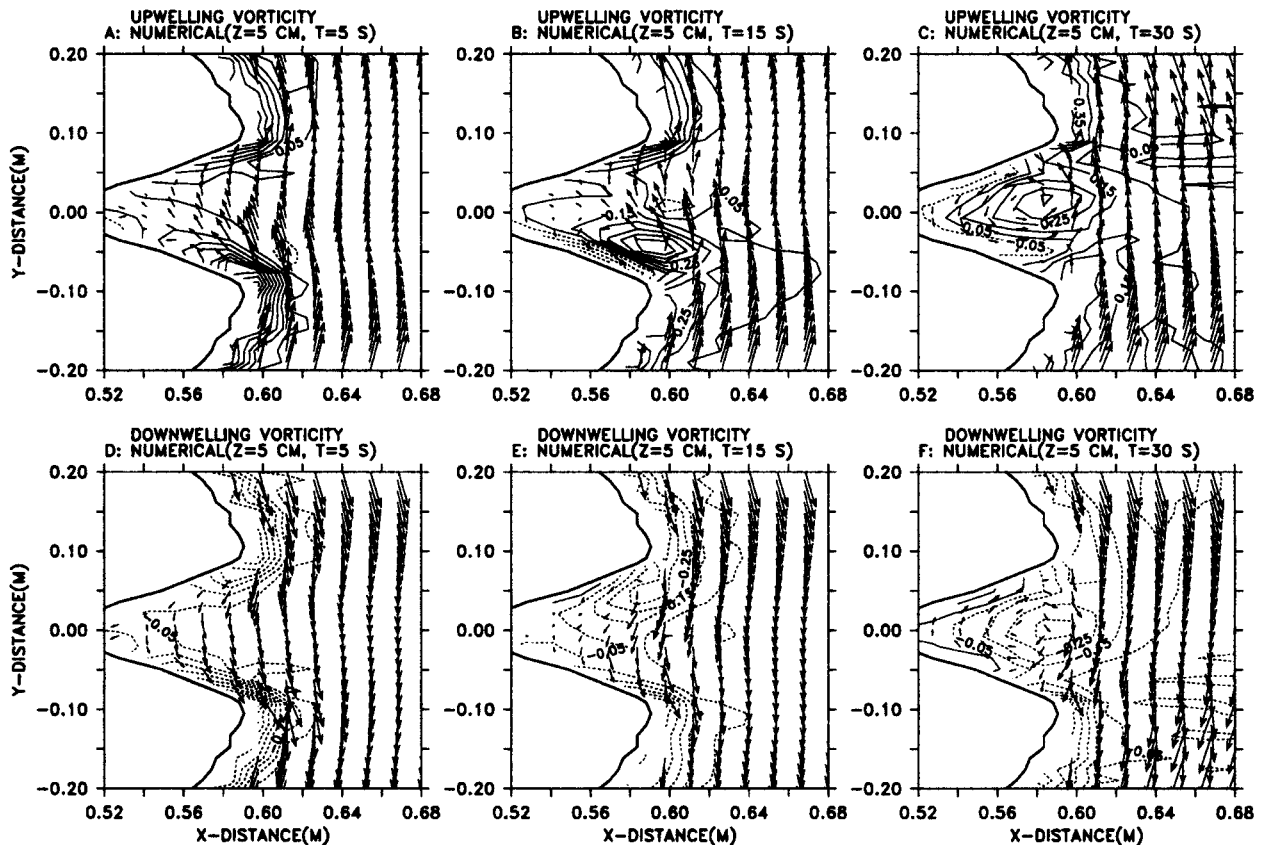


FIG. 12. Time development of the canyon vortices at a depth of 5 cm for the (a)–(c) upwelling and (d)–(f) downwelling cases. Relative vertical vorticity is contoured in units of inverse seconds, with solid lines indicating positive and dashed lines indicating negative relative vorticity.

the first second). Possible reasons for quantitative differences are discussed below.

In the downwelling case (Fig. 14), no strong transient is observed: the quasi-steady downward displacement is reached more or less monotonically. This can be related to the fact that no eddy is generated at the shelf-break level with a downwelling favorable forcing (Fig. 9). The quasi-steady state is characterized by a vertical displacement, which is even smaller than its upwelling counterpart. The agreement between both models is better in the downwelling case, showing that details of the eddy generation process might be responsible for the difference observed in the upwelling case.

Possible factors influencing the quantitative differences between laboratory and numerical displacement time series are as follows. First, although isohalines had larger variation at the head of the canyon and along its walls, it was not feasible to measure at those locales with the laboratory apparatus. The sites measured consequently had displacement signals that proved to be relatively weak and a quantitative difference at those locales does not mean that the whole density field is strongly different in our numerical and laboratory models. Second, displacement values involve the local slope of the vertical density profile $d\rho/dz$ [Eq. (4)]. These

slopes differed from one laboratory experiment to the next (Fig. 2), but a mean slope value was used in the numerical experiments. Third, maximum vertical displacement in the laboratory experiments was always less than the vertical resolution of the model, the latter constrained by computational resources. Furthermore, the numerical results show that larger negative vertical displacements (Fig. 13; $15 < t < 45$ s) occurs in the numerical results just one grid cell (1.4 cm) laterally up canyon, a consequence of the fact that up- and down-canyon isopycnals excursions distances are larger the closer the observation is made to the canyon axis. These considerations could explain much of the difference in the downwelling case (Fig. 14) and some of the difference in the upwelling case (Fig. 13). Nonetheless, the rapidity of the occurrence and relaxation of the negative displacement and the large long-term salinity displacement (Fig. 13) remain unexplainable, the last suggesting a significant, permanent density change at that level. To begin to understand this discrepancy would require higher vertical resolution at the shelf-break level for both laboratory density profiles and for numerical calculations. Consequently, velocities rather than displacements are used here as the primary measure for comparing laboratory and numerical results.

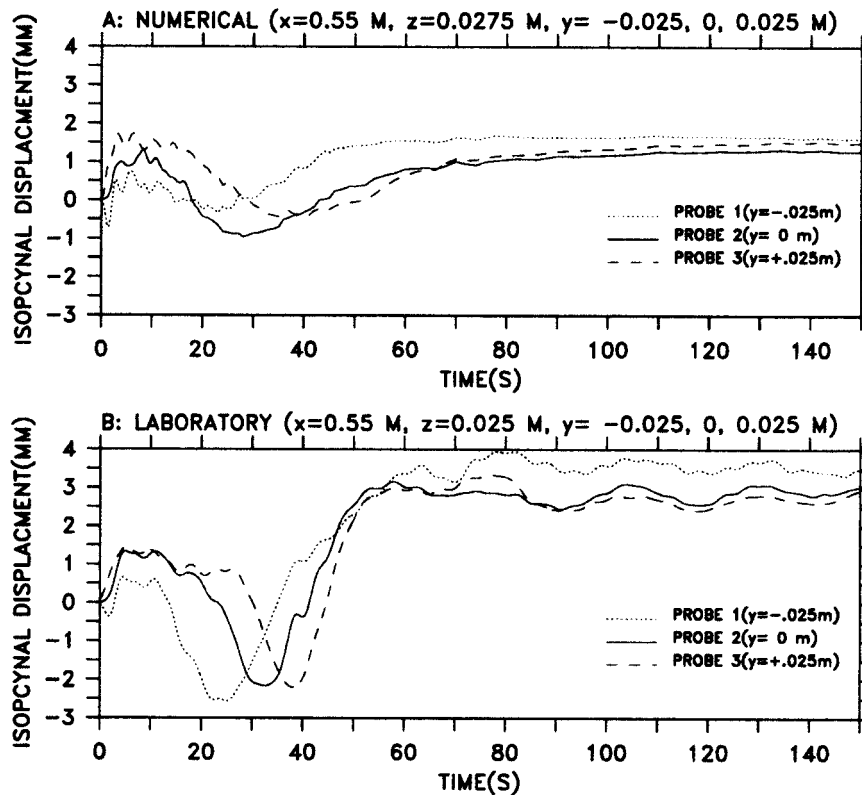


FIG. 13. Upwelling favorable case: time series of density perturbations from the numerical and laboratory models. (a) Time series of isopycnal displacement (see text, section 2a) from the numerical model, at locations 1, 2, and 3 (see Fig. 2a) and $z = z_2$ (see Fig. 2b); (b) the laboratory counterpart of the same time series.

The perturbation of salinity ΔS induced by the motion along the canyon axis at $t = 25$ s and for the upwelling case is seen in Fig. 15a. The maximum ΔS is $\sim 6\%$, located at the canyon head, but the anomaly occurs all the way to the base of the slope. Figure 15a makes clear that the salinity anomaly is trapped along the floor; this explains why the density changes recorded at probe sites (cf. Fig. 3) were consequently small. In order to implement a better sampling scheme, future laboratory experiments could make use of this information provided by the numerical model.

An example of the consequence of upwelling may be seen in the horizontal distribution of salinity anomaly just above shelf depth, after the system has had 25 s to develop (Fig. 15b). Positive salinity anomalies of as much as 3.5‰ are seen on the shelf downstream of the canyon. In an upwelling condition the canyon supplies salt to the shelf, which shelf currents then advect downstream. This higher salinity downstream lens is both quite thin and bottom trapped. The lens's vertical scale may be inferred from the ΔS distribution at $y = 0$, depicted in Fig. 15a.

c. Quantitative comparisons

The agreement between the laboratory and numerical models results can be evaluated by comparing directly

vector plots of the laboratory and the corresponding numerical results, juxtaposed in Figs. 4, 5, 7, 9, and 10. Labels above each square show the time and depth of samples and whether change in rotation has forced an upwelling (Figs. 4, 5, 7, and 10a,b) or downwelling (Figs. 9 and 10c,d) condition. Vector magnitudes and direction over most of the sampled areas are quite comparable, at all depths, over the first 100 s sampled, and for rotation changes of both positive and negative sign. The main systematic difference, occurring within the canyon, appears to be the position of the eddy, which seems to be more sensitive to advection by the large-scale flow in numerical results than in their laboratory counterparts (Figs. 7c,d and 10).

A quantitative way of addressing the agreement between datasets is through a "skill function," which is a statistic that depends on the overall closeness of a given numerical solution to, in this case, the laboratory data. Here we used a skill in the sense defined by Bogden et al. (1996); in order to test the assimilation scheme developed for their model of the Massachusetts Bay, these authors defined the skill S as follows:

$$S = 1 - \frac{\langle [(u_i^L)^2 - (u_i^M)^2] + [(v_i^L)^2 - (v_i^M)^2] \rangle}{\langle [(u_i^L)^2 + (v_i^L)^2] \rangle}, \quad (10)$$

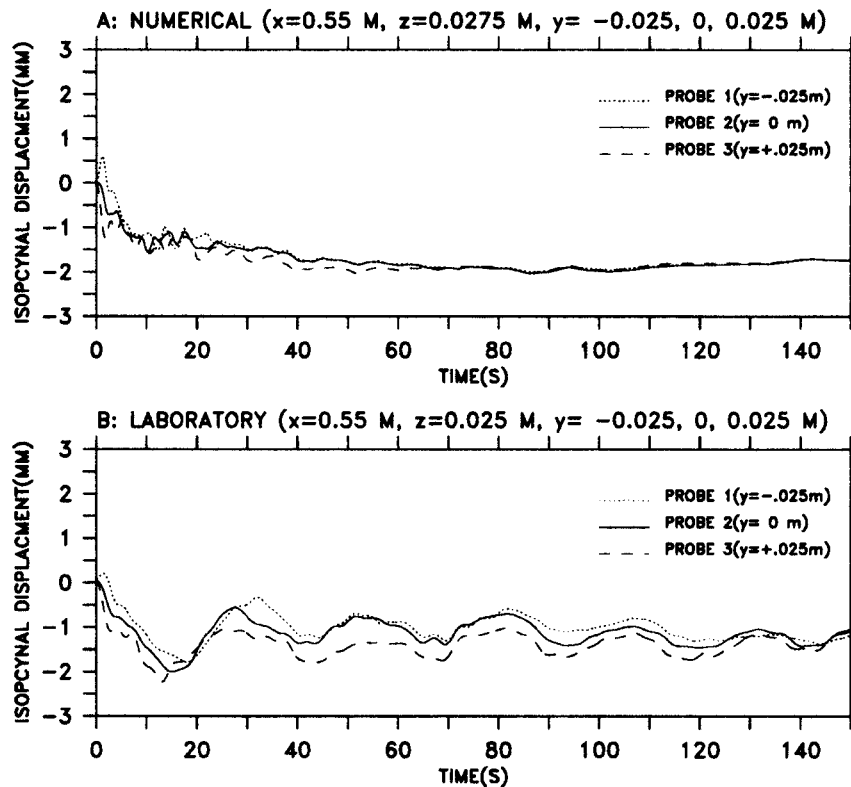


FIG. 14. Downwelling favorable case: time series of density perturbations from numerical and laboratory models (same caption as Fig. 12).

where u_i^L and v_i^L are the laboratory u and v registered at the i th point in space–time, u_i^M and v_i^M are the numerical model u and v registered at the same i th point in space–time, and the angle brackets indicate an average over i . As u_i^L and v_i^L approach u_i^M and v_i^M , skill gets closer to 1. A related measure is the error statistic of Pérenne et al. (1999), where

$$E_R = 2 \frac{\langle [(u_i^L)^2 - (u_i^M)^2] + [(v_i^L)^2 - (v_i^M)^2] \rangle}{\langle [(u_i^L)^2 + (v_i^L)^2] + [(u_i^M)^2 + (v_i^M)^2] \rangle}. \quad (11)$$

The denominator is now the average of the kinetic energy of laboratory and numerical model motion rather than kinetic energy evidenced by the laboratory data alone. It is clear that $S \sim 1 - E_R$. In the following, we compute a second skill statistic $S' = 1 - E_R$ that also tends to 1 in the limit of a perfect match of laboratory and numerical model outcomes.

To not unduly base the score with too many uniform vectors in the abyssal region of the tank, we have confined the computation of S and S' to the wetted region within the boundaries $40 \text{ cm} < x < 63 \text{ cm}$ and $-10 \text{ cm} < y < 10 \text{ cm}$. Numerical model results were regridded to laboratory data locations. The various values of S and S' computed for specific times and measurement levels are listed in Table 1 (upwelling case) and Table 2 (downwelling case).

One sees from these tables that both skill statistics

are comparable in size and range from 84.6% to 98.5%. In neither upwelling nor downwelling cases is there evidence that skill diminishes with simulation time. On the other hand, for the upwelling case only, skill does seem to decrease as depth increases, which could be interpreted by the fact that fewer data points make up the statistic as depth increases. This should also apply to the downwelling case, where no clear trend in S or S' with depth is observed. The (relatively small) decrease of the agreement with depth in the upwelling case, though, does not change the conclusion that skill values must be regarded as high throughout.

4. Conclusions

Laboratory and numerical model data for transient flow in a submarine coastal canyon show good agreement over all observation levels and times sampled. Statistics used to measure the similarity of laboratory and numerical realizations indicate similarity at the 84%–98% level. The close relationship of results was not serendipitous; it came only after a subset of laboratory data was used to show that bottom and interior mixing coefficients in the model had to be represented by molecular values. Larger or smaller bottom stress and fluid viscosity led to model fluid accelerations of a size incommensurate with those observed. Unlike many

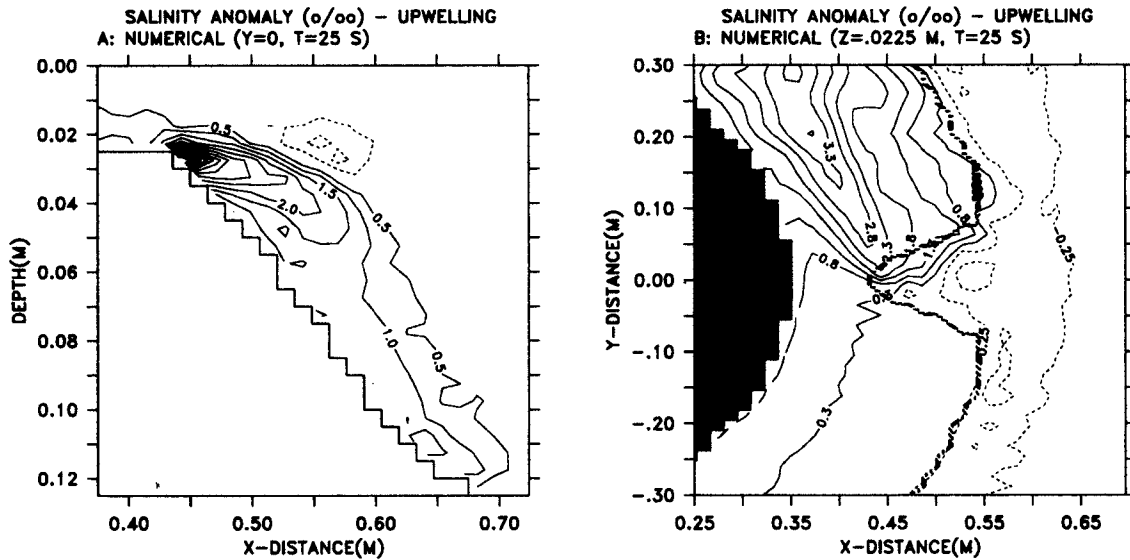


FIG. 15. Salinity field under upwelling favorable forcing at $t = 25$ s (numerical results). The density is represented by the corresponding salinity departure from the state of rest; solid (dashed) lines correspond to positive (negative) values. (a) A vertical cross section along the canyon axis, (b) and a horizontal density field (just above the shelf level). The chain-dotted curve indicates the location of the shelf break.

numerical models, the numerical model used in this study easily handles, in a stability sense, viscosity at molecular magnitude.

In both upwelling and downwelling cases the shelf flow spins down rapidly owing to the shallower depth of that area. This rapid spindown was also observed in the upper layers above the canyon, despite the fact that the canyon is much deeper and that important motions go on inside its walls. This vertical gradient in the velocity field in the canyon area is allowed by the density stratification, which also explain why the shelf flow is only modestly deflected at early times.

For the upwelling favorable case, the flow at the shelf-break level is initially upcanyon over essentially the entire canyon cross section. This flow then evolves into a cyclonic eddy (closed streamlines) that extends deep into the canyon. In the downwelling case, the flow is initially downcanyon and, subsequently, though more slowly than in the upwelling case, an anticyclonic eddy develops. This anticyclonic eddy does not generate closed streamlines at the shelf-break level (as in the

upwelling case) but the vorticity fields reach a near-perfect symmetry as depth increases. The evolution of vorticity in both the laboratory and the numerical results indicates that the vortex in the canyon forms first at the upstream canyon boundary, is detached by flow separation, and subsequently advects into the canyon interior. Vortices in the canyon seen in this study are thus not the direct result of vortex stretching in the canyon as seen in other studies (e.g., Klinck 1996; Hickey 1997).

Stretching of fluid columns initially on the shelf likely produces cyclonic vorticity in both the up- and downwelling cases. This may augment cyclonic vorticity generation by flow separation in the upwelling case. In the downwelling case these two vorticity generation mechanisms would be of opposite sign. These arguments can explain the observed asymmetry in the upper eddy response. Vorticity generation deeper in the canyon is shown to be symmetric with respect to flow direction; cyclonic (anticyclonic) in the upwelling (downwelling) case and is related to flow separation

TABLE 1. Skill scores for the upwelling case. The two values S/S' (see text) are given in percent for various times and depths.

Time	$z = -1.25$ cm	$z = -2.5$	$z = -5$ cm
$t = 10$ s	—	92.8/91.7	—
$t = 20$ s	—	91.9/90.6	—
$t = 25$ s	98.4/98.4	—	86.3/87.6
$t = 30$ s	—	92.7/91.5	—
$t = 40$ s	—	91.9/91.1	—
$t = 50$ s	98.1/98.1	89.3/88.0	84.8/86.5
$t = 75$ s	98.2/98.1	90.6/90.0	93.3/94.2
$t = 100$ s	98.5/98.4	94.0/93.9	84.6/88.1

TABLE 2. Skill scores for the downwelling case. The two values S/S' (see text) are given in percent for various times and depths.

Time	$z = -1.25$ cm	$z = -2.5$ cm	$z = -5$ cm
$t = 10$ s	—	91.8/90.7	—
$t = 20$ s	—	92.7/92.7	—
$t = 25$ s	94.0/93.9	—	93.7/93.1
$t = 30$ s	—	93.9/93.1	—
$t = 40$ s	—	93.3/92.0	—
$t = 50$ s	94.2/93.9	92.1/90.5	91.2/90.5
$t = 75$ s	93.5/92.8	93.8/92.6	88.1/89.3
$t = 100$ s	93.2/92.6	95.1/94.2	90.4/91.3

from the canyon boundary and not local vortex stretching in the canyon.

Laboratory model scales were chosen, as much as possible, for similitude to an idealized coastal ocean canyon. The limitation, of course, is that laboratory flow is laminar, while the ocean is turbulent. Few actual ocean observations are available to compare with present results. Two features inherent in these results and observed in nature are the enhanced upcanyon flows observed in upwelling favorable wind situations (Freeland and Denman 1982) and the development of cyclonic vorticity within the canyon (Hickey 1997).

Overall, our study demonstrates the possibility of interaction between laboratory and numerical model studies of stratified flow over topography. Laboratory data can be used to give a strong test to the quality of a numerical model. Laboratory data like these contain the full effects of nonlinearity, stratification, topography, rotation, bottom friction, and controlled forcing. The last condition is missing in real ocean situations as is, normally, the ability to acquire a dataset of sufficient extent that would allow a numerical model to be well tested. Because flow in the laboratory, as in this case, can be laminar or near laminar, the numerical model can be evaluated in a context that does not have to deal with the confounding problems of turbulence parameterization. Furthermore, because laboratory measurements occur in a closed volume, the corresponding numerical model does not have to address the issue of open boundaries. Laboratory models are thus an excellent source of data for numerical model development and testing, and the intercomparison of the two can lead to higher quality numerical ocean models and data assimilation schemes. The laboratory dataset is freely available to those wishing to test their own models in this way. Just as laboratory results aid numerical model development, numerical results also help interpret laboratory data and can suggest where additional laboratory measurements of high value could be taken. In this sense, laboratory and numerical models can work hand in hand to improve the numerical tools that can then be used on actual ocean problems.

We do not mean to minimize the problem of turbulence when a numerical model is rescaled from laboratory to ocean situations, or the problem of having to deal with open boundaries. Our position is that a numerical model that cannot address data taken under controlled forcing and laminar conditions can surely not address conditions in the real ocean. A satisfactory test against laboratory conditions is necessary, but not sufficient, to guarantee the applicability of a numerical model to the real ocean. Laboratory experiments for turbulent background flow impinging on topography are a next logical step. Such laboratory and numerical model intercomparisons might provide additional insight into effects of turbulence on flow and how turbulence might satisfactorily be parameterized (Boyer and Davies 2000).

Acknowledgments. The laboratory experiments were conducted with the support of the NSF (Grant OCE96-17639). The NOAA VENTS program supported the numerical modeling work. The public domain gridded-data-analyses package Ferret was used for data display and analysis of both numerical and laboratory data.

REFERENCES

- Allen, S., 1996: Topographically generated, subinertial flows within a finite length canyon. *J. Phys. Oceanogr.*, **26**, 1608–1632.
- Arakawa, A., and V. R. Lamb, 1977: Computational design of the basic dynamical processes of the UCLA general circulation model. *Methods of Computational Physics*, J. Chang, Ed., Vol. 17, Academic Press, 173–265.
- Asselin, R., 1972: Frequency filter for time integrations. *Mon. Wea. Rev.*, **100**, 487–490.
- Bogden, P. S., P. Malanotte-Rizzoli, and R. Signell, 1996: Open-ocean boundary conditions from interior data: Local and remote forcing of Massachusetts Bay. *J. Geophys. Res.*, **101** (C3), 6487–6500.
- Bormans, M., and C. Garrett, 1989: A simple criterion for gyre formation by the surface outflow from a strait, with application to the Alboran Sea. *J. Geophys. Res.*, **94**, 12 637–12 644.
- Boyer, D. L., and P. Davies, 2000: Laboratory studies of orographic effects in rotating and stratified flows. *Annu. Rev. Fluid Mech.*, **32**, 165–202.
- , X. Zhang, and N. Pérenne, 2000: Laboratory observations of rotating, stratified flow in the vicinity of a submarine canyon. *Dyn. Atmos. Oceans*, **31**, 47–72.
- Briggs, W. L., 1987: *A Multigrid Tutorial*. Society for Industrial and Applied Mathematics, 90 pp.
- Dalziel, S. B., 1992: Decay of rotating turbulence: Some particle tracking experiments. *Appl. Sci. Res.*, **49**, 217–244.
- Dukowicz, J., and R. D. Smith, 1994: Implicit free surface method for the Bryan–Cox–Semtner ocean model. *J. Geophys. Res.*, **99** (C4), 7991–8014.
- Freeland, H., and K. Denman, 1982: A topographically controlled upwelling center off southern Vancouver Island. *J. Mar. Res.*, **40**, 1069–1093.
- Haidvogel, D. B., and A. Beckman, 1998: Numerical modeling of the coastal ocean. *The Global Coastal Ocean*, Vol. 10, *The Sea—Ideas and Observations on Progress in the Study of the Seas*, K. H. Brink and A. R. Robinson, Eds., John Wiley and Sons, 457–482.
- Harlow, F. H., and J. E. Welch, 1965: Numerical calculation of time-dependent viscous incompressible flow of fluid with free surface. *Phys. Fluids*, **8**, 2182–2198.
- Hickey, B. M., 1997: The response of a steep-sided, narrow canyon to time-variable wind forcing. *J. Phys. Oceanogr.*, **27**, 697–726.
- Kliem, N., and J. D. Pietrzak, 1999: On the pressure gradient error in sigma coordinate ocean models: A comparison with a laboratory model. *J. Geophys. Res.*, **104** (C12), 29 781–29 799.
- Klinck, J. M., 1996: Circulation near submarine canyons: A modeling study. *J. Geophys. Res.*, **101** (C1), 1211–1223.
- McClimans, T. A., J. D. Pietrzak, V. Huess, N. Kliem, J. H. Nilsen, and B. O. Johannessen, 2000: Laboratory and numerical simulation of the Skagerrak circulation. *Contin. Shelf Res.*, **20**, 941–974.
- Pedlosky, J., J. A. Whitehead, and G. Veitch, 1997: Thermally driven motions in a rotating stratified fluid: Theory and experiment. *J. Fluid Mech.*, **339**, 391–411.
- Pérenne, N., J. Verron, D. Renouard, D. L. Boyer, and X. Zhang, 1997: Rectified barotropic flow over a submarine canyon. *J. Phys. Oceanogr.*, **27**, 1868–1893.
- , D. B. Haidvogel, and D. L. Boyer, 2001: Laboratory–numerical model comparisons of flow over a coastal canyon. *J. Atmos. Oceanic Technol.*, **18**, 235–255.
- Sanson, L. Z., and G. J. F. van Heijst, 2000: Interaction of barotropic

- vortices with coastal topography: Laboratory experiments and numerical simulations. *J. Phys. Oceanogr.*, **30**, 2141–2162.
- She, J., and J. M. Klinck, 2000: Flow near submarine canyons driven by constant upwelling winds. *J. Geophys. Res.* **105**, 28 671–28 694.
- Smolarkiewicz, P., and T. L. Clark, 1986: The multidimensional positive definite advection transport algorithm: Further development and applications. *J. Comput. Phys.*, **67**, 396–438.
- UNESCO, 1981: Practical salinity scale 1978 and the international equation of state of seawater. UNESCO Tech. Papers in Marine Science, No. 36, 13–21.
- Wang, J., and M. Ikeda, 1997: Inertial stability and phase error of time integration schemes in ocean general circulation models. *Mon. Wea. Rev.*, **125**, 2316–2327.
- Williams, G. P., 1969: Numerical integration of the three-dimensional Navier–Stokes equations for incompressible flow. *J. Fluid Mech.*, **37**, 727–750.